# scientific reports



# **OPEN**

# The role of Gln269Leu mutation on the thermostability and structure of uricase from Aspergillus flavus

Mona Akhlaghi¹, Bagher Seyedalipour<sup>1⊠</sup>, Mohammad Pazhang² & Mehdi Imani³

Aspergillus flavus Urate oxidase (AFUOX) is promising for potential therapeutic applications, particularly in gout treatment. However, the enzyme's low thermostability and solubility limit its efficacy. A targeted mutation, substituting Gln with Leu at position 269 (Q269L) has been proposed to enhance its stability. The turnover number, catalytic efficiency, and specific activity of Q269L were 3.7 (s<sup>-1</sup>), 53.2 (mM<sup>-1</sup>. s<sup>-1</sup>), and 3.926 U/mg, respectively. In comparison, for the wild type, these were 3.1 (S<sup>-1</sup>), 35.1 (mM<sup>-1</sup>. s<sup>-1</sup>), and 4.018 U/mg, respectively. Notably, the wild type exhibited maximum activity at pH 9 and 25 °C, whereas the activity of Q269L was obtained at pH 9.5 and 30 °C. Furthermore, the half-life of Q269L at 40 °C is significantly longer (85.55 min) compared to the wild-type (49.85 min). The thermodynamic parameters  $\Delta H^z$ ,  $\Delta S^z$ , and  $\Delta G^z$  at 40 °C for Q269L were 60.9 kJ.mol<sup>-1</sup>, -276 J.mol<sup>-1</sup>, and 147.3 kJ.mol<sup>-1</sup>, respectively. Intrinsic fluorescence reductions and ANS fluorescence increases suggest that tryptophan resides in a polar environment with augmented hydrophobic pockets. FTIR analysis of Q269L reveals a decrease in  $\beta$ -sheet and an increase in  $\alpha$ -helix structures, supporting molecular dynamics simulations. Collectively, MD and experimental results underscore Q269L's enhanced thermostability and localized structural alterations, advancing AFUOX's therapeutic potential.

Keywords Uricase, Thermal stability, Q269L mutant, Aspergillus flavus, Molecular dynamics simulation

Urate oxidase (Uricase; EC 1.7.3.3; Uox) is one of the oxidoreductase enzymes<sup>1</sup>, which plays an important role in the path of purine decomposition. Uricase catalyzes the oxidation of uric acid to 5-hydroxyisourate (5-HIU), which spontaneously or enzymatically finally turns into allantoin<sup>2,3</sup>. Uricase is found in many organisms, but it is not expressed in humans and many primates<sup>2</sup>. Two independent nonsense mutations of the uricase gene in stage human evolution and the creation of a premature termination codon have inhibited the expression of this gene<sup>4-7</sup>. The evolutionary loss of uricase expression in humans and certain primates is attributed to a series of genetic mutations that rendered the gene non-functional. The inactivation of this enzyme has resulted in elevated levels of uric acid in the bloodstream, a physiological change that is associated with an increased risk of conditions such as gout. The precise evolutionary drivers of uricase loss remain incompletely understood, but it is thought to be related to dietary changes and adaptations over time<sup>8</sup>. For this reason, the end product of purine metabolism in higher mammals, including humans, is uric acid (UA). While uric acid serves as a potent antioxidant by scavenging free radicals and protecting cells from oxidative damage, its excessive accumulation can lead to metabolic disorders such as gout, hyperuricemia, and metabolic syndrome9. Elevated UA levels are linked to inflammation, insulin resistance, and cardiovascular disease, with research suggesting it may impair endothelial function, disrupt insulin signaling, and alter lipid metabolism, contributing to these conditions. Hyperuricemia, marked by high serum uric acid, is linked to gout, an inflammatory arthritis causing joint pain and swelling. According to data from the US National Health and Nutrition Examination Survey (NHANES) in 2016, the overall prevalence of gout among US adults was 3.9% and 14.6% of the US population is affected by hyperuricemia. These conditions pose significant health and economic challenges, often associated with comorbidities like cardiovascular and kidney disease<sup>10</sup>.

<sup>1</sup>Department of Molecular and Cell Biology, Faculty of Basic Science, University of Mazandaran, Babolsar, Iran. <sup>2</sup>Department of Biology, Faculty of Science, Azarbaijan Shahid Madani University, Tabriz, Iran. <sup>3</sup>Department of Biochemistry, Faculty of Veterinary Medicine, Urmia University, Urmia, Iran. <sup>∞</sup>email: b.alipour81@gmail.com

UA is predominantly present in the human body as free acid and urate salt, both of which exhibit poor solubility in water. Excessive accumulation of UA can lead to hyperuricemia, and in certain cases, the formation and deposition of its crystals result in the development of gout<sup>11</sup>. Several uricase-producing bacterial strains, including *Pseudomonas aeruginosa*, *Proteus mirabilis*, *Streptomyces albusriceolus*, and *Escherichia coli*, as well as fungal species such as *Aspergillus flavus* and *Candida tropicalis*, have been identified<sup>12,13</sup>. *Aspergillus flavus*-derived uricase is preferred for its stability, enhanced catalytic efficiency, specificity for uric acid, a longer half-life and distinct structural features, including disulfide bonds and optimal folding, which preserve its enzymatic activity under diverse conditions. Its structural advantages enable effective uric acid breakdown, reduce accumulation risks, and simplify production and purification<sup>14</sup>. Notably, *Aspergillus flavus*-derived uricase (Uricozyme) has been utilized in hyperuricemia patients to rapidly reduce blood uric acid levels, demonstrating advantages in terms of immunogenicity and solubility compared to bacterial counterparts<sup>15,16</sup>. *Aspergillus flavus*uricase (AFUOX) is composed of four identical monomers, each consisting of 301 amino acids with a molecular weight of 34 kDa<sup>17,18</sup>. AFUOX lacks glycosylation, disulfide bonds, and metal cofactors necessary for its activity<sup>19,20</sup>.

Rasburicase, a pharmaceutical form of recombinant urate oxidase, has proven effective in reducing serum UA concentrations in patients with elevated levels. This recombinant drug is particularly suitable for children with leukemia who experience increased UA levels following chemotherapy, surpassing the efficacy of allopurinol<sup>21,22</sup>. Enzymes possess inherent susceptibility to structural and catalytic modifications, making them promising targets for engineering novel catalytic properties. Recent advancements in molecular biology have enabled the manipulation and selection of genes to enhance enzymatic characteristics and stabilize them. Genetic manipulation is commonly employed to modify amino acid properties, resulting in the creation of new structural-functional features in enzymes<sup>23</sup>. Medicinal proteins often face instability issues, especially thermal instability. To address this challenge, techniques such as genetic manipulation and protein engineering have been employed<sup>24</sup>. Rasburicase is a key therapeutic agent in managing and preventing tumor lysis syndrome (TLS) by converting uric acid into a soluble compound, thus facilitating its excretion and mitigating complications like kidney damage and gout. However, like other medicinal enzymes, Rasburicase's efficacy is impacted by challenges related to enzyme stability<sup>25</sup>. Strategies to enhance its stability include protein engineering techniques such as site-directed mutagenesis (SDM), cloning, random mutagenesis<sup>26–28</sup>, and the use of additives<sup>29</sup>. Maintaining a balance between stability and flexibility is crucial for protein stability. Proteins employ various mechanisms in adverse conditions to preserve the necessary stability and flexibility for maintaining activity, including alterations in protein compaction, charge distribution, hydrophobic surface area, and the ratio of polar, non-polar, acidic, and basic amino acids<sup>30–34</sup>. The low stability of these enzymes poses a significant challenge when utilizing them as protein therapeutics, necessitating the implementation of diverse strategies to improve their stability<sup>24</sup>. Despite its effectiveness, Rasburicase's use requires vigilance due to potential side effects, including allergic reactions, infusion-related events, and hemolysis, particularly in patients with glucose-6-phosphate dehydrogenase (G6PD) deficiency. Therefore, careful patient selection, along with strategies to improve enzyme stability, is critical for optimizing its clinical application<sup>35</sup>.

The present study focuses on Gln269, located within the loop region (Loop 260–277) of Aspergillus flavusuricase, to investigate structural changes and enhance stability. The selection of the Q269 mutation in Aspergillus flavus uricase (AFUOX) was based on several scientific considerations, including modifications in flexible loop regions have been highlighted as a strategy to enhance enzyme thermostability by targeting structural weaknesses<sup>36</sup>. The lack of conservation of Q269 suggests that it may be a promising target for mutagenesis without adversely affecting the enzyme's essential function. Multiple Sequence Alignment (MSA) of uricase sequences from fungi with over 75% similarity, retrieved from the NCBI database and aligned using the UniProt alignment tool, revealed that Q269 is not conserved across the studied sequences. Detailed sequence information for uricase homologs, including their respective IDs, is provided in Supplementary Fig. S1 and Table S1. The selection of Q269 was guided by its potential contribution to protein stability based on established principles of protein engineering. Factors such as hydrophobicity, reduced susceptibility to degradation-sensitive residues such as cysteine, asparagine, and glutamine and enhanced electrostatic interactions have been shown to improve stability  $^{37-39}$ . As such, deamidation of glutamine residues, such as Q269, was hypothesized to improve the thermal stability of AFUOX through its structural stabilization effects, supported by  $\Delta\Delta G$ -based computational predictions and targeted mutagenesis studies<sup>40</sup>.

Gln269 was selected due to its proximity to Leu262 and Leu268 (Fig. 1), potentially leading to unfavorable interactions between the polar side chains of Gln269 and the non-polar side chains of Leu262 and Leu268. Each active site is formed at the bottom of a funnel-shaped pocket at the dimer interface, created by the flexible linker between strands S7 and S8, the coiled region (residues 153–178), and their symmetrical counterparts. The 15 conserved residues near the active site, including Lys10, Thr57, Arg176, Gln228, Asn254, and His256, may influence enzyme function, while Pro284 and Gly286 likely contribute structurally to the active site conformation. Leu170 and Phe159 form a hydrophobic environment beneath the substrate, with Leu170 aiding substrate positioning, though Asn51 and Ser226 have no defined role in enzyme function. Such interactions destabilize Loop 260–277, consequently impacting the overall stability of the enzyme. By replacing Gln269 with Leu through site-directed mutagenesis, it is hypothesized that these unfavorable interactions can be reduced, ultimately increasing the stability of uricase. The study aims to explore the structural, functional, and catalytic characteristics of the enzyme, as well as investigate the effects of the Gln269 to Leu substitution on *Aspergillus flavus* uricase stability. Additionally, computational methods, including molecular dynamics simulations, were employed to analyze and compare the structural alterations between the wild-type AFUOX and the mutant enzymes.

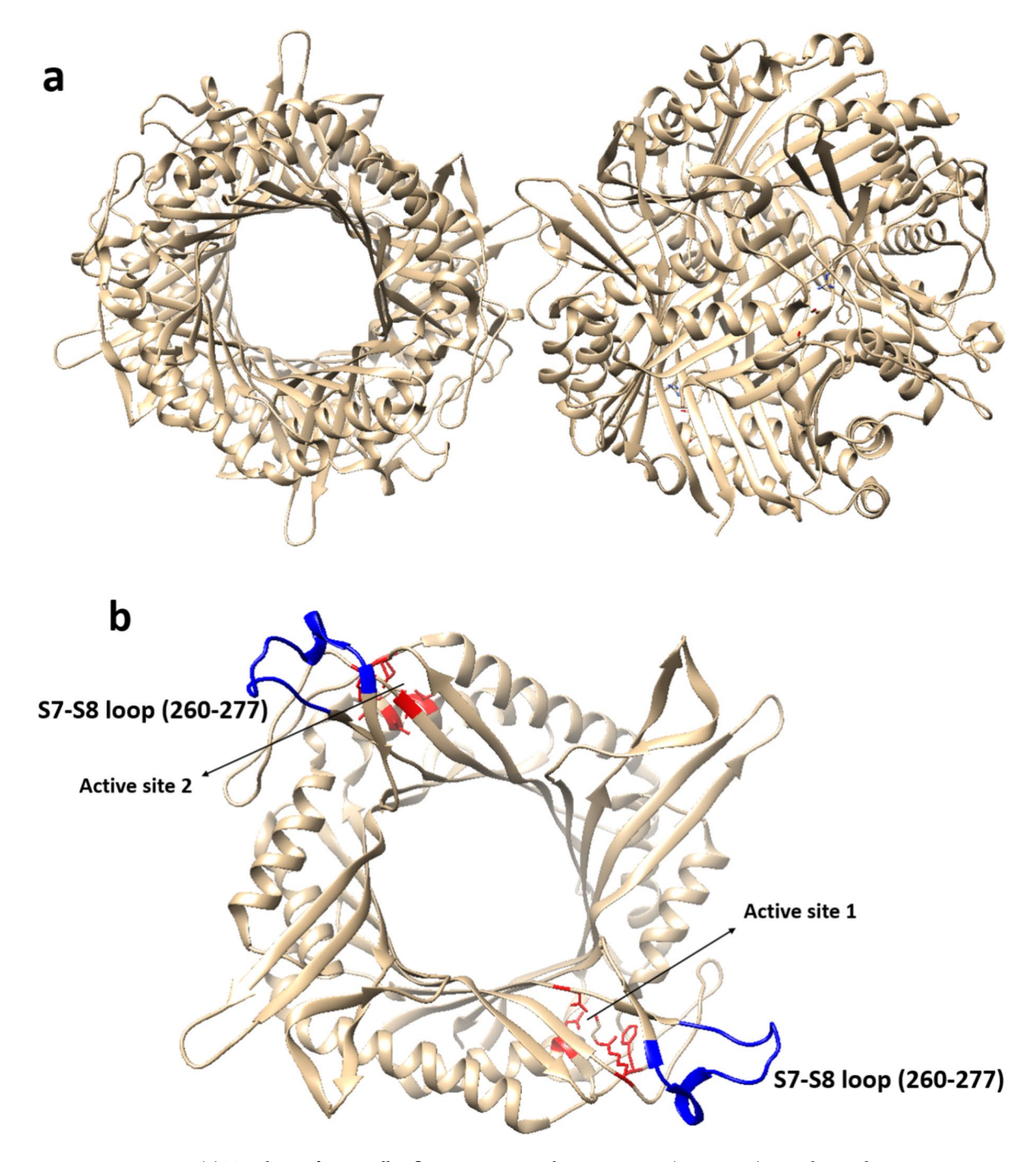


**Fig. 1.** (a) Topology of *Aspergillus flavus* uricase as a homotetramer (PDB: 1r56) was obtained using UCSF Chimera software. (b) The dimer structure of the UOX enzyme, active site residues (1 and 2), and the S7-S8 loop (260–277) are drawn in red and blue, respectively. (c) The monomer structure of *Aspergillus flavus* uricase enzyme (Chain A) at residue position 269. Glutamine residue 269 (in red) is in contact with the other indicated residues. By substituting glutamine with leucine at position 269, asparagine 274 contacts leucine 269. The yellow line indicates contact between residues.

# Materials and methods Computational study

Predicting structural stability and activity performance

The Stability Changes ( $\Delta\Delta G$ ) calculations of the I-Mutant2, i-Stable, and DUET servers assessed the effect of mutation on the AFUOX stability and structure. These calculation servers could provide a report of the free energy change as a series of positive and negative values to stabilize and destabilize mutations, respectively<sup>41</sup>.

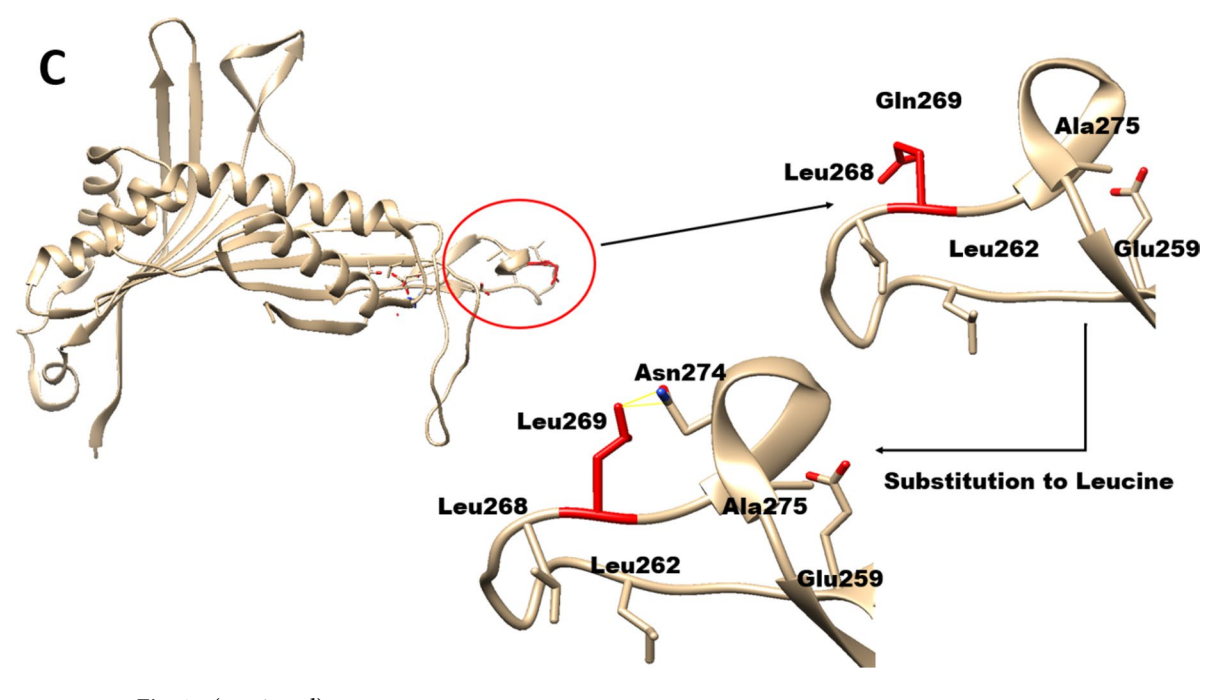


Fig. 1. (continued)

#### Molecular dynamics (MD) simulation

The initial structure of *Aspergillus flavus*uricase (AFUOX) for molecular dynamics (MD) simulations was obtained from the Protein Data Bank (PDB) with the identifier 1R56, which had a resolution of 2.30 Å<sup>42</sup>. In this study, the PDB file with the code 1R56 was retrieved, and the Q269L mutation was introduced using Pymol software. MD simulations of both the wild-type AFUOX (WT-AFUOX) and the Q269L mutant were conducted using the GROMACS 2016.4 package<sup>43</sup> and the Amber ff99SB force field<sup>44</sup>. The Tip3p water model was chosen as the solvent for the simulation, and the protein was placed in a triclinic box. To neutralize the two negative charges of the protein, two sodium (Na) atoms were added to the box, resulting in box dimensions of 92.1 \* 70 \* 93.2. The structure was energy-minimized using the steepest descent algorithm with a time interval of 0.01, and the minimization process was stopped when the maximum force reached a value less than 1000 kJ/mol/nm.

To control the simulation temperature and pressure under isotropic conditions, the Berendsen thermostat and Parrinello-Rahman barostat were employed. The system underwent equilibration runs under constant number, pressure, and temperature (NPT) conditions for 1 ns and 2 ns until reaching a temperature of 298 K and a pressure of 1 bar<sup>45</sup>. The initial velocities for the MD simulation were generated using the V-Rescale thermostat based on the Maxwell distribution. During the equilibration runs of constant number, volume, temperature (NVT), and NPT, position constraints were applied. The MD simulation utilized the leap-frog algorithm to integrate Newton's equations with a time step of 2 fs, and data were collected every 10 ps. Covalent bonds within the WT-AFUOX and Q269L mutant proteins were constrained and fixed during the MD run using the linear constraint solver (LINCS) algorithm. The Particle-Mesh Ewald (PME) method was employed to handle long-range electrostatic interactions<sup>46</sup>.

Subsequently, MD simulations of the equilibrated system were performed for a total of 60 ns, allowing all atoms to freely move. The MD trajectories were analyzed using GROMACS distribution programs. Various parameters such as solvent accessible surface area (SASA), root mean square deviation (RMSD), root mean square fluctuation (RMSF), radius of gyration (Rg), and hydrogen bonds were calculated. The secondary structure elements of both WT-AFUOX and the Q269L mutant were analyzed using the dictionary of secondary structure protein (DSSP) program.

#### **Experimental section**

#### Material

Qiagen supplied the Ni–NTA agarose resins, while Merck supplied 1-Anilinonaphthalene-8-sulfonate (ANS). The following materials were purchased from Bio Basic: agarose, yeast extract, tryptone, boric acid, uric acid, sodium acetate, Glycine, KOH, isopropyl-β-D-thiogalactopyranoside (IPTG), kanamycin, and phenolmethyl-sulfonyl fluoride (PMSF). The dialysis tubing cellulose membrane (12,400 Da cutoff) was procured from Sigma, all SDS-PAGE chemicals were purchased from Merck, Thermo Scientific supplied *HL Taq* DNA polymerase and *Dpn I*, and Bioneer (Korea Southern) supplied the plasmid extraction kit.

#### Site-directed mutagenesis

The Aspergillus flavus UOX gene (Accession number; X61766.1) was retrieved from Genbank and synthesized by Bioneer, then cloned into the pGEM-B1 vector. The bacterial codon-optimized synthetic coding DNA sequence

of the *Aspergillus flavus* uricase was subsequently cloned into pET- 28a (+) vector using endonuclease restriction sites for *NcoI* and *XhoI*, resulting in the construct pET-28a(+)-AFUOX<sup>47</sup>. For site-directed mutagenesis, the coding sequence of *Aspergillus flavus* uricase (AFUOX) was synthetically prepared, optimized, and used as a template as previously described<sup>48</sup>. The recombinant pET-28a (+) vector containing the AFUOX gene (pET28a-AFUOX) served as the template. Quik-Change PCR site-directed mutagenesis was performed to construct the single-point mutation Q269L. Two mutagenesis primers were designed for Q269L: a forward primer (5′-AAG GGT CTG CTG AAT ACC GGT AAA AAT GCG GAG G-3′) with the mutation site highlighted, and a reverse primer (5′-GC ATT TTT ACC GGT ATT CAG CAG ACC CTT ATG CC-3′) also with the mutation site highlighted. The Quik-Change PCR reactions were conducted using *HL Taq* DNA polymerase (Thermo Scientific) with the following cycling parameters: pre-denaturation at 95 °C for 5 min, followed by 20 cycles of 95 °C for 45 s, 69.2 °C for 45 s, and extension at 72 °C for 8 min. The PCR product was digested with Dpn I (Thermo Scientific) to eliminate methylated parental plasmid DNA. The pET-28a (+)-AFUOX plasmids were then transformed into *E. coli* DH5α cells through heat shock at 42°C for 90 s. The recombinant vector containing the mutant pET-28a (+)-AFUOX was extracted using a plasmid miniprep extraction kit (Bioneer, Korea Southern), and after confirming the sequencing accuracy, it was transformed into the expression strain BL21.

#### Expression and purification of WT- AFUOX and Q269L mutant

For the expression and purification of WT-AFUOX and the Q269L mutant, a 5 ml LB medium containing 50  $\mu$ g/ml kanamycin was inoculated with a fresh single recombinant colony and cultured overnight at 37 °C with shaking at 160 rpm. Subsequently, 100 ml of LB medium with 50  $\mu$ g/ml kanamycin was inoculated with 500  $\mu$ l of the bacterial culture and incubated at 37 °C with vigorous shaking until the optical density (OD600) reached approximately 0.6–0.8. The cells were induced with IPTG (0.8 mM) and lactose (8 mM) for protein expression in recombinant cells for 6 h at 37 °C and 220 rpm. After induction, the cells were collected by centrifugation at 5000 rpm for 25 min at 4 °C. The cell pellet was resuspended in a cold lysis buffer (50 mM NaH2PO4, 300 mM NaCl, 10 mM imidazole, pH 7.8) containing 1 mM PMSF and 1 mg/mL lysozyme, followed by sonication (8 cycles of 20 s on, 40 s off). The cell extracts were centrifuged at 12,000 rpm for 25 min at 4 °C, and the supernatant containing the recombinant protein was collected. The recombinant protein was then purified using Ni–NTA agarose affinity chromatography with a 2 mL elution buffer (50 mM NaH2PO4, 300 mM NaCl, 250 mM imidazole, pH 8). The purified recombinant protein was dialyzed twice against 20 mM borate buffer (pH 8.5), and the protein concentrations were determined using the Bradford method. Analysis of the purified proteins was performed using a 12.5% SDS-PAGE gel.

#### Uricase activity assay, optimum temperature and pH, and kinetic parameters

For the uricase activity assay, the optimum temperature and pH, and kinetic parameters, a reaction mixture containing 270  $\mu$ L of 20 mM boric acid buffer (pH 8.5), 100  $\mu$ M uric acid, and 15  $\mu$ L of the purified uricase solution (0.02 mg/mL) was incubated at 25 °C for 6 min. The reaction was terminated by adding 15  $\mu$ L of 20% (w/v) KOH<sup>49</sup>. Uricase activity was measured at 293 nm using  $\epsilon$ 293 = 12.600 M<sup>-1</sup> cm<sup>-1</sup>. One unit of uricase activity was defined as the amount of enzyme required to produce 1  $\mu$ mol of uric acid into allantoin per minute at pH 8.5 and 25 °C. Then, Specific activity was expressed as U/mg and was calculated using the following Eq. (1):

$$Specific \ activity \left( \frac{U}{mg} \right) = \frac{(\Delta A293/minTest - \Delta A293/minBlank)(df)(Vt)}{12.6 \times Vs \times [E]}, \tag{1}$$

where df is the dilution factor, and  $\epsilon 293 = 12.600 \text{ M}^{-1} \text{ cm}^{-1}$  is the extinction coefficient of uric acid at 293nm.

To determine the optimum temperature, the purified UOX enzyme was incubated at temperatures between 0 and 60 °C at intervals of 5 °C for 6 min. The reaction was halted by the addition of 20% (w/v) KOH. The enzyme activity was measured by monitoring the absorbance at 293 nm. The relative activity was expressed as a percentage of the maximum activity achieved. To determine the optimal pH for uricase enzyme activity, various buffers were prepared, including Glycine (200 mM), Phosphate (200 mM), Acetate (200 mM), and Borate (50 mM). The pH levels of these buffers were adjusted within the range of 4 to 12.5, with increments of 0.5 pH units. Enzyme activity at each pH was assessed by adding 30  $\mu$ L of the substrate to 255  $\mu$ L of the respective buffer. Subsequently, 15  $\mu$ L of the enzyme solution (0.02 mg/ml) was added, and the absorbance at 293 nm was measured using a spectrophotometer.

The maximum rate of absorbance decrease per minute was calculated based on the double reciprocal plot method, which was used to determine the kinetic parameters  $K_m$  and  $V_{max}$  for both WT-AFUOX and the mutant. The enzyme activity was measured at 25 °C for 6 min, with absorbance readings at 293 nm taken every 30 s. The turnover number ( $k_{cat}$ ) was calculated by dividing the  $V_{max}$  value by the concentration of the purified enzyme and its molecular weight.  $K_m$  was calculated using the Lineweaver–Burk plot method.

### Fluorescence spectroscopy and dynamic quenching

Fluorescence measurements were conducted using a Fluorescence Spectrofluorometer (FP-8300; Jasco) at room temperature to investigate intrinsic and extrinsic fluorescence properties. After dialyzing the purified UOX, the intrinsic fluorescence was recorded using a concentration of 0.02 mg/ml UOX in a borate buffer (20 mM, pH 8.5). The excitation wavelength was set at 295 nm, and the emission spectrum was scanned from 300 to 450 nm. The excitation and emission slit widths were adjusted to 5 nm and 10 nm, respectively. Extrinsic fluorescence analysis was performed using the ANS probe, which binds to hydrophobic pockets. The concentration of the purified enzyme was maintained at 0.02 mg/ml, while the ANS probe was used in varying concentrations of 10,

20, 30, 40, 50, and  $60 \,\mu\text{M}$ . Fluorescence emission spectra were recorded from 370 to 700 nm with an excitation wavelength of 350 nm<sup>50</sup>. The excitation and emission slit widths were set to 5 nm and 10 nm, respectively.

Fluorescence quenching studies using acrylamide as a neutral quencher were performed to investigate the microenvironment of tryptophan residues. According to Ciono and colleagues research, different amounts of the acrylamide quencher (ranging from 0 to 900 mM,) were added to enzyme solutions (20  $\mu$ g/ml) in a borate buffer (20 mM, pH 8.5)<sup>51</sup>. The fluorescence of Trp residues was observed by exciting the samples at a wavelength of 295 nm, and the emission spectra were monitored from 300 to 450 nm. Quenching analysis was determined using the Stern–Volmer equation as follows<sup>52</sup>:

$$F_0/F = 1 + Ksv[Q] \tag{2}$$

where F<sub>0</sub> and F are fluorescence intensities in the absence and presence of a quencher, respectively, Ksv is the Stern–Volmer quenching constant; [Q] is the concentration of the quencher.

#### FTIR and circular dichroism (CD) spectroscopic studies

Far-UV CD spectra were recorded at room temperature using a spectropolarimeter (Jasco-810, Tokyo, Japan). The measurements were conducted in the wavelength range of 190 nm to 260 nm, with a protein concentration of 0.25 mg/ml in a 20 mM borate buffer at pH 8.5. A 1 mm path-length quartz cell was used for the measurements. Fourier-transform infrared spectroscopy (FTIR) analysis of the protein secondary structure was performed using a BRUKER TENSOR 27 instrument in Germany. KBr tablets were used for sample preparation. At a resolution of 4 cm<sup>-1</sup>, the infrared spectra were captured in the wave number range of 400–4000 cm<sup>-1</sup>. For the analysis, protein samples with 0.9 mg/ml of concentration were used. Using OriginPro 2021 software, the raw spectra acquired in the amide I region (1600–1700 cm<sup>-1</sup>) were analyzed. For quantitative investigation of protein secondary structures, curve fitting of the amide I region FTIR data is frequently used. When examining the elements in the Amide I band, overlapping peaks in the Amide I area are frequently shown using Fourier Self-Deconvolution (FSD) and second derivative spectra<sup>53</sup>.

#### Time-dependent thermal inactivation and thermodynamic parameters

To determine the thermal inactivation, purified UOX is incubated at different temperature ranges (30, 40, 50, and 60 °C) for 60 min with an interval of 5 min at the desired temperature. It was then transferred to ice for 30 min to obtain the folded structure. After half an hour, it was re-incubated for 5 min at room temperature and the activity was measured by monitoring absorbance at 293 nm as described above. The residual activity was expressed as a percentage of the original activity. To calculate the inactivation rate constant ( $K_{\rm in}$ ) (Eq. 3) and half-life, first-order kinetics (Eq. 4) suggests that the reaction happens at one inactivation rate in a single step. The inactivation rate constant was determined as the slope of the direct dependence of the natural logarithm of the residual activity on time by linear regression.

Thermal inactivation of enzymes can be investigated by a first-order reaction (Eq. 3):

$$\operatorname{Ln}\left(\frac{\operatorname{At}}{\operatorname{A0}}\right) = -K_{\operatorname{in}}t,\tag{3}$$

where  $A_t$  is the activity of the protein at time t,  $A_0$  is the initial enzyme activity and  $k_{in}$  is the protein inactivation rate constant at the studied temperatures. The half-life time of the protein is calculated by the inactivation rate constant (Eq. 4).

$$Halflife = \frac{0.693}{\text{Kin}}. (4)$$

To describe the temperature effect on the inactivation rate constants using the Arrhenius equation<sup>54</sup>, the activation energy can be estimated by linear regression analysis of the natural logarithm of the rate constant versus the reciprocal of the absolute temperature.

$$LnK = LnA - \frac{Ea}{RT},$$
(5)

where k and R are the inactivation rate constant and universal gas constant, respectively. A,  $E_{a_i}$  and T represent the Arrhenius constant, activation energy, and the absolute temperature in Kelvin, respectively (Eq. 5).

The  $E_a$  and A values were determined from the slope and the intercept of the Arrhenius plot, respectively<sup>55</sup>. To determine thermodynamic parameters, using the transition state theory, the values of enthalpy ( $\Delta H^{\pm}$ ) and entropy ( $\Delta S^{\pm}$ ) have been calculated expressions<sup>56</sup>. The value of  $\Delta S^{\pm}$  can be obtained from the slope of the dependence of  $\Delta G^{\pm}$  on temperature according to the equation:

$$\Delta H^{\neq} = Ea - RT \tag{6}$$

$$\Delta S^{\neq} = R \left( LnA - Ln \frac{KB}{h} - LnT \right) \tag{7}$$

$$\Delta G^{\neq} = \Delta H^{\neq} - T \Delta S^{\neq} \tag{8}$$

where h and  $k_B$  indicate the Planck's constant (6.624×10<sup>-34</sup> J.s) and the Boltzmann's constant (1.381×10<sup>-23</sup> J.K<sup>-1</sup>), respectively.

#### Chemical denaturation studies of UOX: thermodynamic stability

To assess the thermodynamic stability of the samples, guanidine hydrochloride (GdnHCl) was employed as a chemical denaturant. A 10 M GdnHCl stock solution was prepared in a 20 mM borate buffer with pH 8.5. Purified samples of UOX and the mutant were mixed with increasing concentrations of GdnHCl ranging from 0 to 8 M. These mixtures were prepared in the presence of a 20 mM borate buffer with pH 8.5<sup>57</sup>. The final protein concentration in each sample was 0.08 mg/ml. The samples were thoroughly mixed and subsequently incubated for 24 h at 4°C<sup>58</sup>. Fluorescence emission spectra of the samples were recorded using a Jasco Fluorescence Spectrofluorometer (FP-8300). The excitation wavelength was set at 295 nm, and the emission spectrum was scanned from 300 to 450 nm. To determine the standard Gibbs free energy of denaturation ( $\Delta G^0$ ), the fluorescence intensity data was plotted against the GdnHCl concentration. The two-state transition model was utilized for this analysis. The following Eq. (9) was used to calculate the equilibrium constant in each concentration of GdnHCl through the fluorescence data<sup>59</sup>:

$$k = \frac{YF - Yobs}{Yobs - YU} \tag{9}$$

where  $Y_{obs}$  is the value of the measured parameter (such as absorbance or fluorescence),  $Y_F$  is its value in the folded state, and  $Y_U$  is its value in the unfolded state.  $Y_F$  and  $Y_U$  values were obtained from the extrapolation of lines to zero concentration of GdnHCl.

The difference in free energy between the folded and the unfolded states ( $\Delta G^0$ ) was calculated using Eq. (10):

$$\Delta G^0 = -RT \ln K \tag{10}$$

where T and R show the absolute temperature (in Kelvin) and the gas constant (8.314 J.mol $^{-1}$  K $^{-1}$ ), respectively.  $\Delta G^0$  varies linearly with [GdnHCl] denaturant, which can then be used to determine the free energy difference at 0 M GdnHCl,  $\Delta G^0_{\rm H2O}$ , assuming a linear dependence of free energy with GdnHCl concentration, m, according to the equation $^{60}$ . Then the plot was drawn against the concentration of GdnHCl $^{59}$ . The equation of the resulting line is in the form of Eq. (11).

$$\Delta G^0 = \Delta G_{\rm H2O}^0 - m \times [\text{denaturant}] \tag{11}$$

where  $\Delta G^0$  is the free energy of denaturation at each concentration of guanidine hydrochloride, m is the slope of the line and a measure of the solvent accessibility during protein folding and denaturation, and  $\Delta G^0_{H2O}$  is the free energy of protein denaturation in water, the value of which is linearity is obtained up to zero concentration of guanidine hydrochloride.

# Results and discussion

# Prediction of single mutation effects on mutant protein stability

Bioinformatic methods were employed to assess the stability of the mutant enzyme structure. The i-Stable, DUET, and PremPS integrated servers were utilized to predict the stability of the mutant enzyme structure in comparison to the wild type. These integrated computing servers are specifically designed to predict how mutations can impact the stability, structure, and function of proteins. Through analysis of various factors, including physicochemical and evolutionary properties, these servers provide accurate predictions regarding the effects of mutations on proteins<sup>41</sup>. Of particular interest from an experimental standpoint is the free energy difference between the Q269L mutant and WT-AFUOX proteins. Equation (1) ( $\Delta\Delta G^u = \Delta G^u_{mutant} - \Delta G^u_{wild-type}$ ) represents the disparity in unfolding free energy between the Q269L mutant and WT-AFUOX proteins of  $\Delta\Delta G$  indicates if the variation decreases ( $\Delta\Delta G^u < 0$ ) or increases ( $\Delta\Delta G^u > 0$ ) the protein stability. These servers illustrate the variation in free energy change ( $\Delta\Delta G$  or ddG) between the Q269L mutant and WT-AFUOX protein, where positive values indicate stabilizing mutations and negative values indicate destabilizing mutations. Consequently, the outcomes from all servers for the Q269L mutant demonstrate an increment in stability, as evidenced by the positive free energy values (Table S2).

#### MD simulations

MD simulations are computational methods that simulate the interactions between atoms and molecules based on classical physics principles. These simulations calculate the precise positions and relative velocities of each atom over time<sup>65</sup>. In this study, MD simulations were employed to investigate the structure of the WT-AFUOX and Q269L mutant enzymes and their relationship with enzyme stabilization. The protein sequence alignment results indicated that Q269 is not conserved in uricase from different sources and, therefore has no critical role in the inter-subunit interactions in tetrameric uricase. Also, Native PAGE analysis indicated that the oligomerization state of Q269L was similar to the WT-AFUOX and no significant effect on the oligomerization state of the enzyme was observed, as provided in Supplementary Fig. S2. Similarly, the results of molecular dynamics simulation on monomers, both the WT-AFUOX and Q269L mutant enzymes, have been confirmed by the experimental results. The mentioned reasons decline the importance of molecular dynamics simulation results on tetrameric uricase and make it unnecessary for this study.

The RMSD was utilized to assess the flexibility of  $C\alpha$ -atoms in the backbone between WT-AFUOX and the Q269L mutant. The RMSD, obtained using the least square fit method, serves as a suitable measure to evaluate the convergence time of the protein to a stable position<sup>66</sup>. As depicted in (Fig. 2a), the simulation initially exhibits

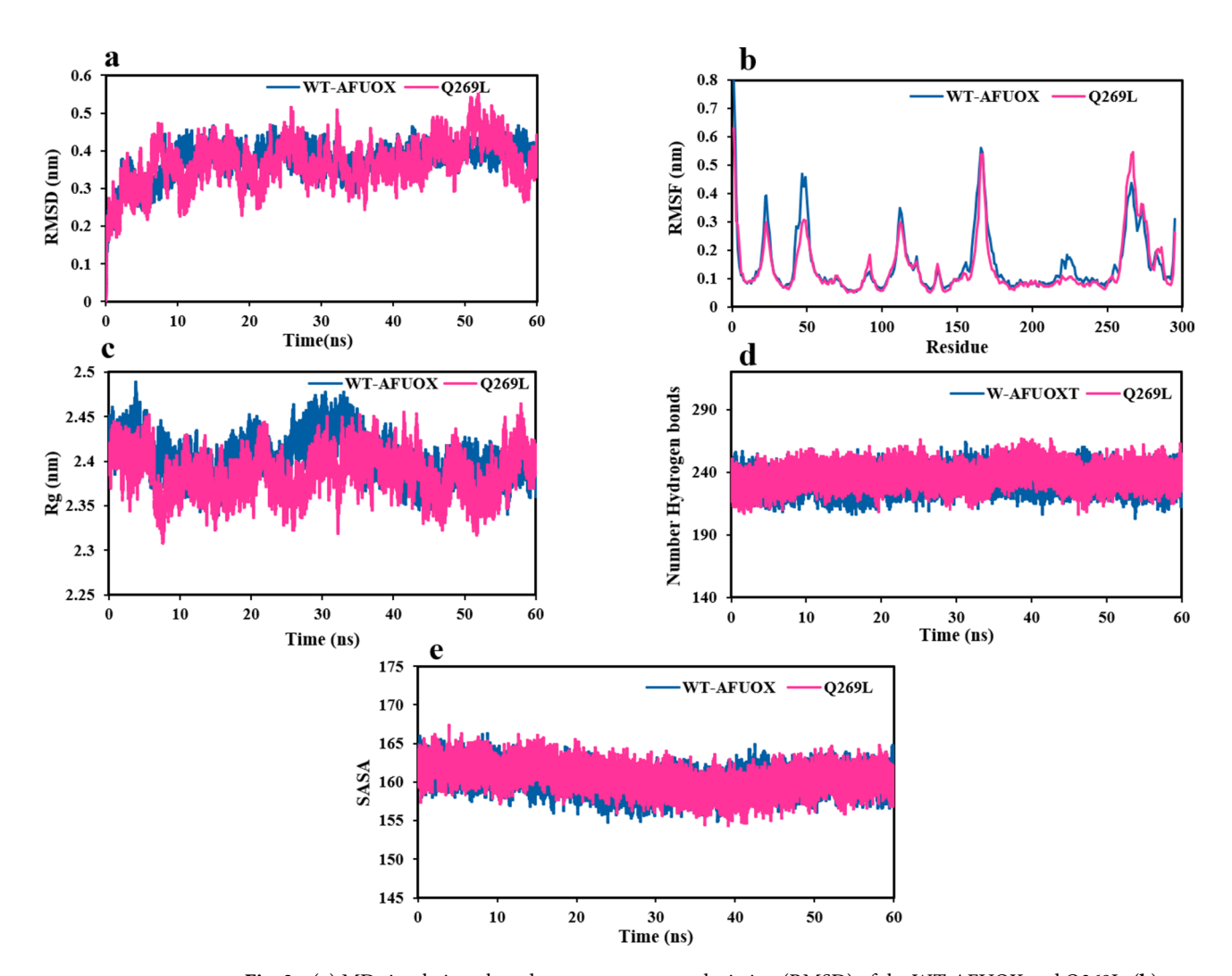


Fig. 2. (a) MD simulations-based root-mean-square deviation (RMSD) of the WT-AFUOX and Q269L, (b) root-mean-square fluctuation (RMSF) of the backbone  $C\alpha$ -atoms of the WT-AFUOX and Q269L, (c) Radius of gyration (Rg) of the WT-AFUOX and Q269L, (d) The number of hydrogen bonds of the WT-AFUOX and Q269L during the simulation time, and (e) Solvent accessible surface area (SASA) value of the WT-AFUOX and Q269L mutant during 60 ns of the MD simulation period.

a sudden increase with a steep slope. However, throughout the simulation, minimal changes in protein stability are observed, indicating that the structures remain in a stable state. The average stability changes for WT-AFUOX and the mutant proteins were determined to be  $(0.37\pm0.044)$  nm and  $(0.36\pm0.058)$  nm, respectively. The results of the RMSD changes indicate that the mutant structure, compared to the wild type, experiences reduced structural fluctuations, leading to increased stability. In other words, the RMSD of the mutant reaches equilibrium at lower values compared to WT-AFUOX. Our analysis demonstrates that each system was simulated for a sufficient duration to achieve equilibrium, allowing the capture of all relevant conformational states. RMSD, as a metric, reflects the deviation of a protein's conformation from its initial state, and its consistently low value in the mutant underscores the structural integrity retained in the enzyme during the simulation timeframe. The slightly lower C $\alpha$ -RMSD values observed in the mutant enzyme compared to the wild type (WT) throughout the simulation indicate that the mutant maintains a more stable overall structure, which is a hallmark of enhanced protein stability.

To analyze the flexibility and dynamics of WT-AFUOX and the Q269L mutant proteins along the MD trajectory, the RMSF was employed. The RMSF evaluates the flexibility of protein residues, with curved peaks indicating regions of increased flexibility. Increased values suggest enhanced flexibility but reduced stability. As shown in (Fig. 2b), the average flexibility for WT-AFUOX and the mutant Q269L protein were  $(0.15\pm0.11)$  nm and  $(0.13\pm0.1)$  nm, respectively. The RMSF values for the WT-AFUOX and mutant at residue 269 were 0.33 nm and 0.41 nm, respectively. The mutation at position 269 likely induces a local effect, increasing the flexibility of that region compared to WT-AFUOX. However, overall, the decrease in mutant flexibility, as indicated by RMSF in all residues, signifies an increase in stability compared to WT-AFUOX. This finding is consistent with results obtained from bioinformatics servers  $^{68}$ . Additionally, RMSF analyses provide further support for the enhanced stability of the mutant enzyme. Regions with lower RMSF values demonstrate reduced atomic-level

fluctuations, indicative of greater rigidity and stability in those regions. The mutant enzyme consistently displayed lower RMSF values across key residues, highlighting the stabilization effect introduced by the mutation. These results collectively suggest that the mutation contributes to the structural and functional stability of the enzyme. Low RMSD and RMSF values indicate the enzyme's structural integrity and that its active site is stable, which is essential for its catalytic function. Stability is crucial for the enzyme to effectively bind substrates and carry out its biochemical reactions. These changes were added to the revised manuscript<sup>69</sup>.

The Rg is utilized to assess protein compactness since determining the relative distance of each atom to the center of protein mass is challenging  $^{70}$ . (Fig. 2c) illustrates the behavior of all structures during the simulation, showing convergent and similar patterns. A slight decrease in the mutant is observed from 25 to 35 ns, after which the structures remain in a floating and stable state. The average Rg values for WT-AFUOX and the mutant Q269L protein were determined as  $(2.4\pm0.023)$  nm and  $(2.38\pm0.023)$  nm, respectively. The changes in compactness in the Q296L mutant were higher than those in WT-AFUOX, indicating enhanced structural resistance and compactness in the mutant compared to WT-AFUOX. A more compact protein structure often reflects enhanced structural stability, essential for maintaining the enzyme's active site. Stability minimizes the likelihood of denaturation or unfolding, particularly under physiological or stress-inducing conditions, thereby preserving enzymatic activity. A compact structure may promote tighter binding through closer interactions between the enzyme and uric acid, potentially stabilizing substrate binding or critical transition states. Compactness may also impose structural constraints that limit functional adaptability, underscoring the delicate interplay between protein structure and enzymatic performance  $^{71}$ .

Hydrogen bond formation is a crucial indicator of bond strength and stability in chemical structures, playing a significant role in protein stability<sup>72</sup>. The hydrogen bond changes curve was employed to assess the number of hydrogen bonds in WT-AFUOX compared to the Q269L mutant, providing an estimation of protein stability. As shown in (Fig. 2d), the average number of hydrogen bonds for WT-AFUOX and Q269L were 233 ± 7 and 237 ± 7, respectively. In the Q269L variant, a slight increase in the average number of hydrogen bonds was observed, critical for structural integrity. Hydrogen bonds likely contribute to a more compact and stable protein conformation, enhancing its resilience to environmental factors such as temperature and pH fluctuations. Increased hydrogen bonding also has implications for enzyme activity, by stabilizing the protein structure, better equipped to maintain its active conformation, ensuring that the active site remains correctly oriented for substrate binding and catalysis. This structural stability can lead to enhanced enzymatic efficiency by preserving the integrity of key catalytic residues. However, while increased hydrogen bonding can reduce excessive flexibility, which might destabilize the enzyme, it must not overly rigidify the structure. Thus, the observed increase in hydrogen bonding in the Q269L variant likely strikes a balance, improving stability and potentially augmenting catalytic activity without compromising the enzyme's necessary dynamic properties73. Although these changes are partial and local, they can significantly affect the stability of the structure and enzyme activity. Thus, hydrogen bonds and hydrophobic interactions are considered the main driving forces for protein folding and stability<sup>42</sup>.

The SASA is commonly used to evaluate protein-solvent interactions  $^{74}$ . SASA values reflect the conformational stability of the enzyme, indicating the extent of protein interaction with its environment over time. An increase in SASA suggests protein unfolding and exposure of buried residues. The WT-AFUOX and Q269L mutant exhibit SASA values of  $160.234 \pm 1.4$  and  $160.489 \pm 1.6$ , respectively (Fig. 2e). The results demonstrate no significant changes in SASA values for the mutant enzyme compared to WT-AFUOX. Additionally, the secondary structure elements of the enzyme were analyzed using the DSSP program, and the details of the WT-AFUOX protein and its mutant's secondary structure contents are presented in (Table 1). For the WT-AFUOX protein, the contents of  $\alpha$ -helix and  $\beta$ -sheets were determined as 23% and 40%, respectively, while for the mutant, they were 24% and 36%, respectively. The decrease in  $\beta$ -sheets and the increase in  $\alpha$ -helices may contribute to maintaining the integrity of the enzyme's active site and potentially lead to increased activity. Previous studies have reported that the conversion of  $\beta$ -sheets to random coils can enhance enzyme activity. This study suggests that mutations in WT-AFUOX cause changes in its secondary structure content, potentially affecting intermolecular hydrogen bonds and  $\alpha$ -helix content compared to the wild-type form, which is consistent with previous studies  $^{69,75,76}$ .

# Expression and purification of AFUOX protein

Primer design was done after mutation selection and mutagenesis was carried out using the Quick-change PCR method on the pET-28a (+)-AFUOX gene as a template by *HL Taq* DNA polymerase enzyme. Then, the PCR product was digested with Dpn1 enzyme for 18 h. The pET-28a (+)-AFUOX was transformed into DH5 $\alpha$  cells and finally, the plasmid was extracted and the sequencing was determined. To optimally express the AFUOX enzyme, a 2xyt culture medium was used along with an IPTG inducer at a concentration of 0.8 mM and 8 mM lactose. The samples were incubated for 6 to 8 h at 37°C with a shaker at 220 rpm. In this study, AFUOX was overexpressed and purified by Ni–NTA agarose affinity chromatography. The purity of the UOX enzyme was checked on 12.5% SDS-PAGE gel and the approximate weight of the protein was estimated to be 34 kDa, which

Secondary structure	Coil	β-Sheet	β- Bridge	Bend	Turn	A-Helix	3-Helix
WT-AFUOX	19%	40%	1%	6%	9%	23%	2%
Q269L	22%	36%	2%	7%	7%	25%	1%

**Table 1.** Percentages of secondary structure elements of WT-AFUOX and Q269L mutant using the DSSP program.

showed a high degree of purity, which can be seen in (Fig. 3)<sup>77</sup>. Protein concentration by the Bradford method and using protein Bovine serum albumin as a standard was determined<sup>78</sup>.

# Kinetic properties assay

The catalytic rates of purified WT-AFUOX and Q269L mutants were examined at varying substrate concentrations. The specific activity of WT-AFOX and the Q269L mutant was determined to be approximately 4.018 U/mg and 3.926 U/mg, respectively. This disparity can likely be attributed to the local structural effects of the mutation and the reduction in flexibility, which aligns with the findings from molecular dynamics simulations. To ascertain the optimum temperature for WT-AFUOX and the Q269L mutant, enzymatic assays were conducted at different temperatures. The maximum activity of WT-AFUOX was observed at 25 °C, while for the mutant, it was at 30 °C. Notably, an increase in temperature resulted in a decline in enzyme activity. Furthermore, the optimal pH for WT-AFUOX and the Q269L mutant was determined to be 9 and 9.5, respectively.

The kinetic parameters ( $K_m$  and  $k_{cat}$ ) of WT-AFUOX and the Q269L mutant were calculated through least-squares analysis using Lineweaver–Burk plots. The obtained kinetic parameters for WT-AFOX and the Q269L mutant are shown in (Table 2). The  $K_m$  values for WT-AFOX and the Q269L mutant were measured as 0.089  $\mu$ M and 0.07  $\mu$ M, respectively. The results showed that Q269L mutanton has a higher affinity to uric acid compared to WT-AFOX. The turnover number ( $k_{cat}$ ) of the Q269L mutant was found to be approximately the same as that of WT-AFUOX, implying no significant increase in turnover number values for the Q269L mutant compared to WT-AFUOX. Additionally, the catalytic efficiency ( $k_{cat}/K_m$ ) of WT-AFUOX and the Q269L mutant was compared by calculating the  $k_{cat}/K_m$  ratio. The Q269L mutant demonstrates an approximately 1.5-fold increase in kinetic efficiency compared to WT-AFUOX, as shown in (Table 2)<sup>79</sup>.

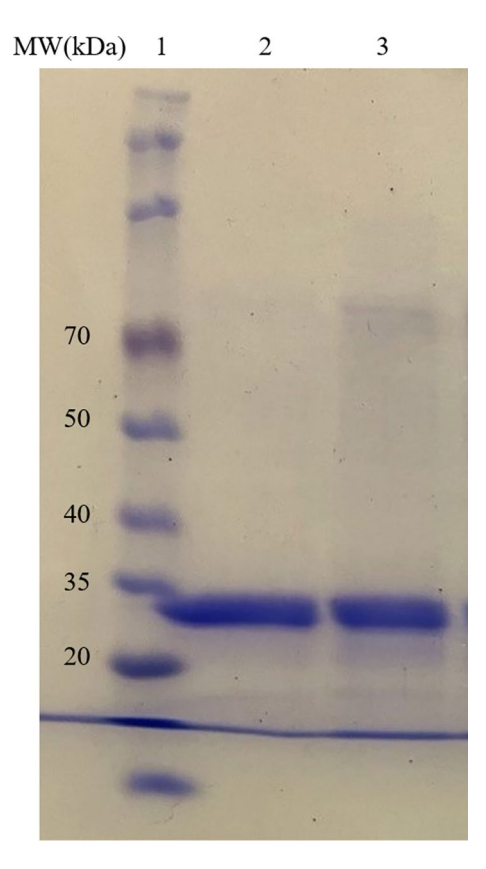


**Fig. 3.** SDS-PAGE analysis of the overexpressed and purified enzyme (12.5% polyacrylamide gel). Lane 1 shows molecular weight markers, and lanes 2 and 3 show purified UOX mutant using Ni–NTA affinity chromatography.

	Km (mM)	Specific activity (U/mg)	K <sub>cat</sub> =TON (sec <sup>-1</sup> )	$K_{cat}/Km$ $(mM^{-1}. S^{-1})$
WT-AFUOX	$0.089 \pm 0.034$	$4.018 \pm 0.243$	3.125 ± 0.061	$35.112 \pm 2.80$
Q269L	$0.070 \pm 0.016$	3.926 ± 0.129	3.725 ± 0.087	53.217 ± 4.19

**Table 2.** Kinetic parameters of WT-AFUOX and Q269L mutant.

Values are means  $\pm$  the standard deviation of three independent measurements. The kinetic parameters of the purified uricase solution (0.02 mg/mL) for both the WT-AFUOX and Q269L mutant were measured after incubation at 25 °C for 6 min. The turnover number ( $K_{cat}$ ) was calculated by dividing the  $V_{max}$  value by the concentration of the purified enzyme.

#### Calculation of time-dependent thermal inactivation

Figure 4 depicts the plot of % residual activity against time to analyze the thermal inactivation kinetics of WT-AFUOX and the mutant at temperatures of 30 °C, 50 °C, 40 °C, and 60 °C. The results demonstrate that the Q269L mutant, after incubation for 5 to 60 min within the temperature range of 30–60 °C, retains 82%, 47%, 18%, and 14% of its initial activity, respectively. In comparison, the WT-AFUOX enzyme maintains 72%, 43%, 5%, and 2% of its initial activity during the same time intervals. The kinetic stability and half-life of the enzyme were calculated by fitting a natural logarithmic curve of the remaining enzyme activity over time, following a first-order reaction pattern for enzyme inactivation. This analysis revealed a linear decrease in enzyme activity over time. The half-life, which serves as a measure of kinetic stability, significantly increased in the mutant compared to the wild type when examined within the temperature range of 30–60°C.

Thermodynamic stability was assessed using the Arrhenius equation, as shown in (Fig. 5). The results indicate that the mutant enzyme exhibits improved stability and a delay in thermal denaturation compared to the wild type. According to the data in (Table 3), the activation energy ( $E_a$ ) for WT-AFUOX and the Q269L mutant was determined to be 64.1 kJ/mol and 63.5 kJ/mol, respectively. The increase in  $E_a$  suggests a higher sensitivity of the reaction to temperature changes. Consequently, the Q269L mutant displays greater tolerance to high temperatures compared to WT-AFUOX. The Gibbs free energy, a thermodynamic parameter indicating the spontaneity of inactivation processes and the energy barrier for enzyme deactivation, was also evaluated. An increase in Gibbs free energy signifies greater enzyme stability. In thermal deactivation reactions,  $\Delta H \neq \text{indicates changes in protein configuration and protein-protein interactions such as hydrogen bonding, electrostatic interactions, and van der Waals forces. Positive values of <math>\Delta H \neq \text{in both states indicate that uricase denaturation is an endothermic reaction. } \Delta S \neq \text{reflects the degree of randomness, conformational changes, and flexibility of the enzyme structure. Changes in the natural structure of the enzyme molecule, such as unfolding or folding, impact <math>\Delta S \neq \text{. Overall}$ , the evaluation of  $\Delta H \neq \text{. } \Delta S \neq \text{. }$  and  $\Delta G \neq \text{ values indicates that the Q269L mutant enhances thermal stability, reduces conformational changes during thermal inactivation, and exhibits higher thermal stability compared to WT-AFUOX.$ 

Furthermore, one of the reasons for the irreversible inactivation of proteins is the deamidation of asparagine and glutamine residues, leading to their conversion into aspartic acid and glutamic acid, respectively. This deamidation introduces negative charges that disrupt the native protein structure. By replacing the glutamine residue in the uricase enzyme with leucine, the risk of deamidation is eliminated, resulting in increased enzyme stability against irreversible inactivation.

# Calculating thermodynamic stability by GdnHCl

To investigate the impact of mutants on the thermodynamic stability of the UOX protein, the guanidine hydrochloride (GdnHCl) denaturant was employed. The plot in (Fig. 6a) exhibits a sigmoidal shape, indicating a

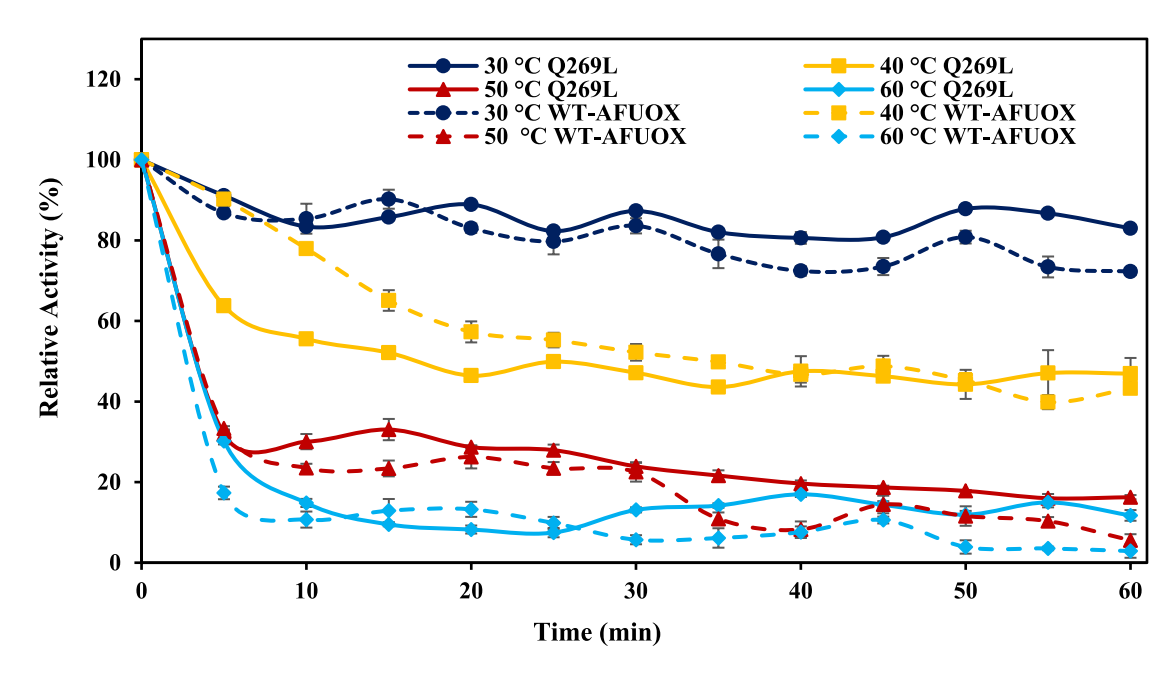


**Fig. 4.** Time-dependent temperature inactivation curves for the WT-AFUOX and Q269L were analyzed at different times (0–60 min) and four different temperatures: 30 °C (light blue), 40 °C (yellow), 50 °C (red), and 60 °C (dark blue).

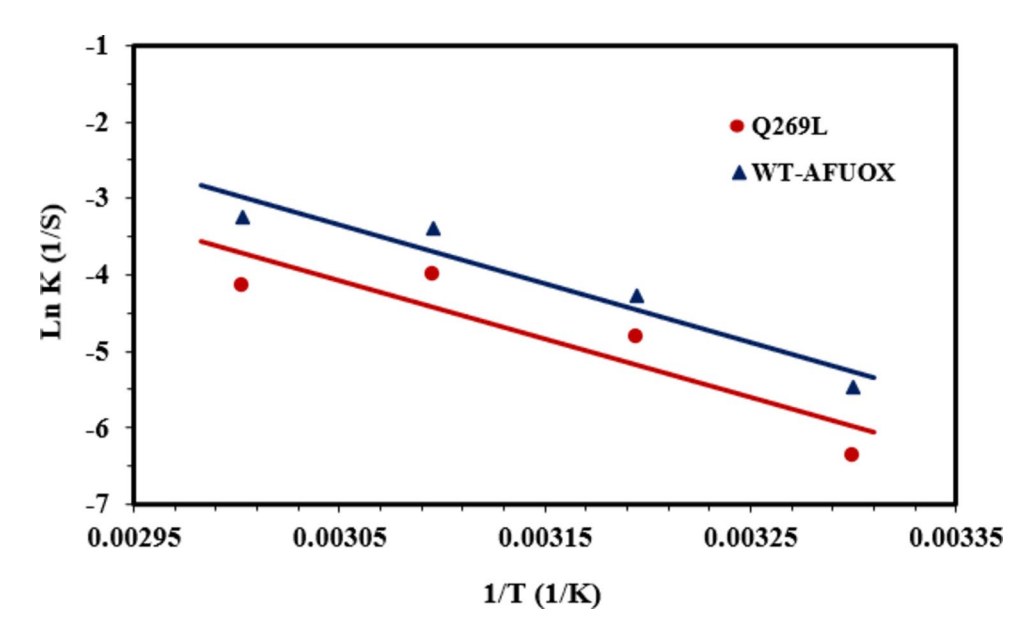


**Fig. 5.** Arrhenius plots for calculating enthalpy and entropy of uricase inactivation WT-AFUOX and Q269L mutant. Error bars represent the standard deviation among three replicates. See Section "Time-dependent thermal inactivation and thermodynamic parameters" for more details.

	Ea (KJ.mol <sup>-1</sup> )	T (K)	ΔH (KJ.mol <sup>-1</sup> )	$\Delta S (J.mol^{-1}k^{-1})$	ΔG (KJ.mol <sup>-1</sup> )	Half-life (min)
WT-AFUOX	64.1	303	61.58	-266.6	142.3	161.16
		313	61.5	-266.9	145	49.85
		323	61.4	-267.1	147.7	20.625
		333	61.3	-267.4	150.3	17.81
Q269L	63.55	303	61	-275.8	144.6	407.647
		313	60.9	-276	147.3	85.55
		323	60.8	-276.3	150.1	37.86
		333	60.7	-276.5	152.8	43.86

Table 3. Thermodynamic parameters for thermal inactivation and half-life of UOX at different temperatures.

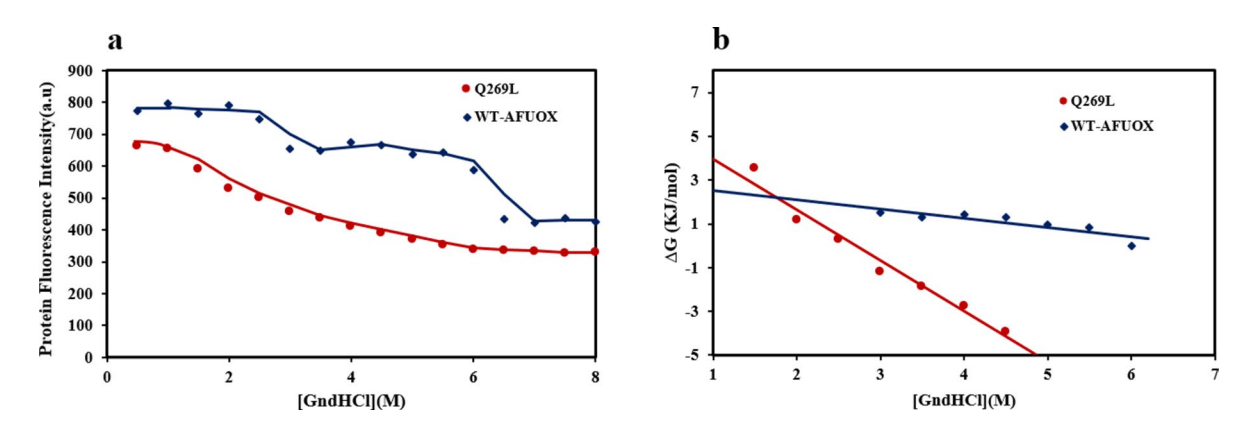


**Fig. 6.** Fluorescence emission spectra of (a) WT-AFUOX and Q269L in the range of 0–8 M Gdm.HCl and protein concentration 0.08 mg/ml in 20 mM borate buffer and pH 8.5. Thermodynamic stability of (b) WT-AFUOX and Q269L against different Gdm.HCl concentrations (0–8 M). See Section "Chemical denaturation studies of UOX: Thermodynamic stability" for more details.

two-state transition and a decrease in emission intensity with increasing GdnHCl concentration. By utilizing the equilibrium constant derived from these plots, the free energy was calculated for each concentration of GdnHCl. Subsequently, the thermodynamic parameters of denaturation against GdnHCl concentration were obtained from the plotted data (Fig. 6b). The values of m and  $\Delta G^0$  H<sub>2</sub>O were determined through extrapolation methods (Table S3). The results indicate that the mutant protein exhibits greater thermodynamic stability compared to WT-AFUOX, with  $\Delta G^0$  H<sub>2</sub>O N  $\rightarrow$  D values of 2.2 kJ/mol and 4 kJ/mol for the WT and mutant, respectively.

Chemical denaturants like GdnHCl are commonly employed to induce protein unfolding and study protein folding under laboratory conditions. However, the precise mechanism of protein denaturation by chaotropic agents such as GdnHCl remains unclear. GdnHCl interacts with backbone amide groups and polar side chains, forming multiple hydrogen bonds. Additionally, it increases surface pressure, leading to the desalting of the aqueous phase. It is hypothesized that GuH+readily adsorbs onto the protein surface due to its hydrogen bonding capability and weakens electrostatic interactions. Such a mechanism could explain the differential denaturation caused by GdnHCl. Even at various concentrations, denaturants can form multiple hydrogen bonds and participate in van der Waals interactions with the polypeptide backbone and protein side chain groups, which restrict molecular motion 80-82.

#### CD and FT-IR measurements

The Far-UV CD spectrum of WT-AFUOX and Q269L was analyzed at a concentration of 0.25 mg/ml and a temperature of 25°C, as depicted in (Fig. 7a). The results indicate a change in the secondary structure of the protein. Both samples exhibited a negative ellipticity peak at 217 nm, associated with  $\beta$ -sheet secondary structure. However, the Q269L mutant displayed additional negative ellipticity peaks at 208 nm and 222 nm, as well as a positive ellipticity peak at 193 nm, indicative of  $\alpha$ -helical structural elements. A comparison of the two spectra revealed an increased magnitude of the positive and negative signals corresponding to  $\alpha$ -helical structural elements in the Q269L mutant compared to WT-AFUOX.

Quantitative analysis of protein secondary structures often utilizes curve fitting of the Fourier-transform infrared spectroscopy (FTIR) spectrum in the amide I region (1700–1600 cm<sup>-1</sup>). Fourier self-deconvolution (FSD) or second derivative spectra are commonly employed to resolve overlapping peaks associated with different secondary structures<sup>84</sup>. These FSD regions or second derivative spectra correspond to specific types of secondary

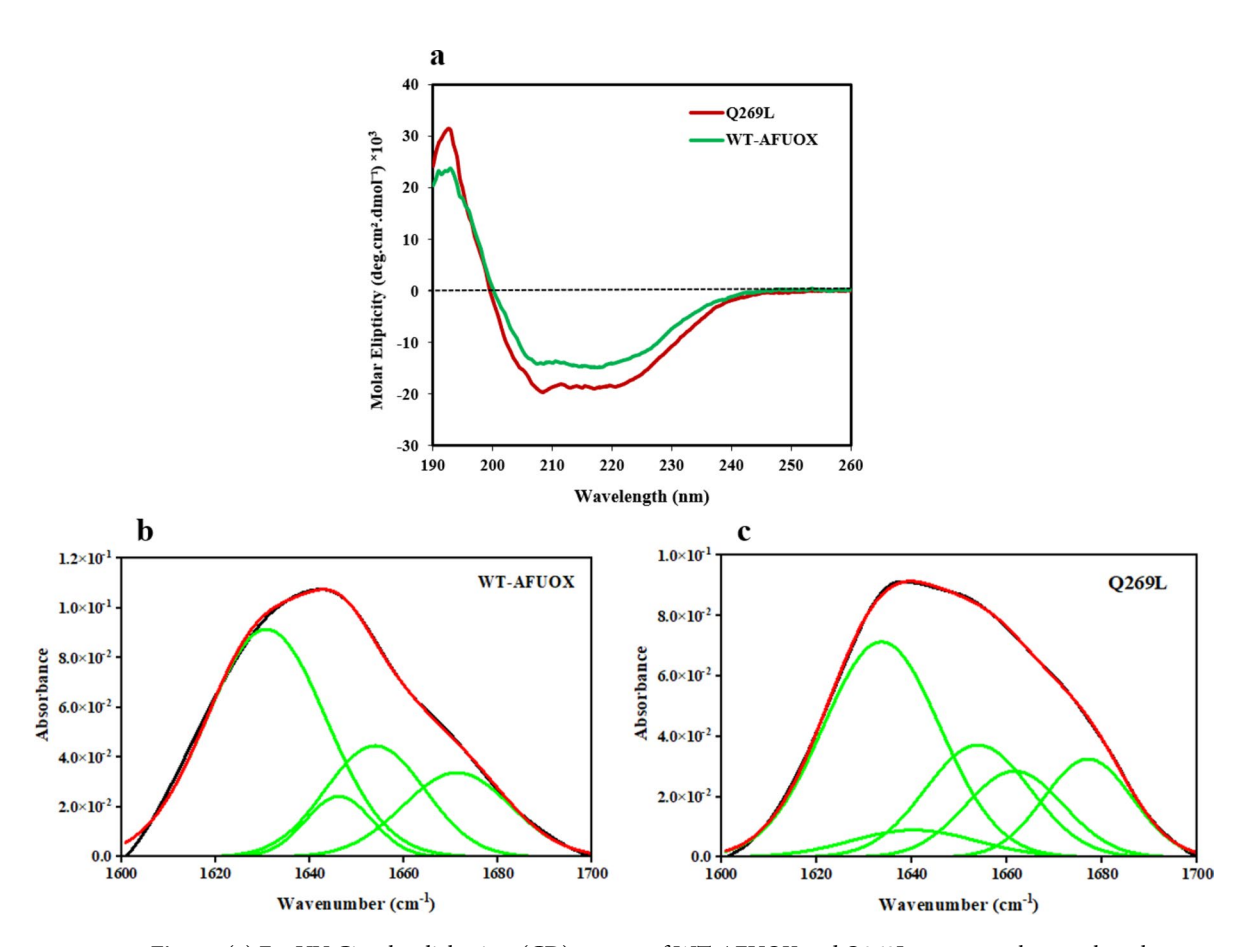


**Fig. 7.** (a) Far UV Circular dichroism (CD) spectra of WT-AFUOX and Q269L mutant at the wavelength range of 190–260 nm. The concentration of protein was 0.25 mg/ml in borate buffer (20 mM, pH 8.5 and 25 °C). Results of a Fourier self-deconvolution (FSD) analysis on the amide I (1700–1600 cm $^{-1}$  region) for (b) WT-AFUOX and (c) Q269L mutant. The assignment of different peaks to different secondary structure elements is shown. Protein concentration was 0.9 mg/ml in 20 mM borate buffer (pH 8.5 and 25 °C).

structure components. The FTIR spectrum of WT-AFUOX and the Q269L mutant, with a concentration of 0.9 mg/ml in 20 mM borate buffer at pH 8.5 and 25°C, was analyzed using the Fourier self-deconvolution method, as shown in (Fig. 7 b,c).

(Table 4) presents the peak positions and percentages of each secondary structure type obtained from the deconvolution of the Amide I band. The amide I spectrum assigns the parallel  $\beta$ -sheet structures to the range of 1623–1641 cm<sup>-1</sup>, while anti-parallel  $\beta$ -sheet structures are assigned to 1623–1641 cm<sup>-1</sup> and 1670–1695 cm<sup>-1</sup>. The  $\alpha$ -helix structure exhibits peak frequencies in the range of 1648–1660 cm<sup>-1</sup>, random coil structures in the range of 1639–1657 cm<sup>-1</sup>, and  $\beta$ -turn structures in the range of 1662–1686 cm<sup>-1</sup> s<sup>85–87</sup>. The deconvolution of the Amide I peak revealed a secondary structure composition of 52%  $\beta$ -sheet for the WT and 44%  $\beta$ -sheet for the mutant, indicating a decrease in  $\beta$ -sheet content in the mutant enzyme. Additionally, the percentage of  $\alpha$ -helix was higher in the mutant (35%) compared to the wild type (21%), as shown in (Table 4). These FTIR spectrum results align with the findings of the molecular dynamics simulations regarding the secondary structure analysis.

# Fluorescence analysis

The fluorescence technique was employed to examine local changes in the tertiary structure of the protein. The distinct property of protein intrinsic fluorescence arises from the sensitivity of tryptophan residues to their surrounding environment. Alterations in fluorescence emission can be attributed to the positioning of tryptophan in either a hydrophilic or hydrophobic environment. Introducing a new residue through mutation can affect the local environment around the indole tryptophan ring. In this study, the intrinsic fluorescence spectrum was excited at a wavelength of 295 nm, and the emitted fluorescence was analyzed.

It is worth noting that AFUOX contains seven tryptophan residues/subunits: Trp186, Trp188, and Trp208, which are embedded within the core of each monomer; Trp160 and Trp174, which are exposed to the solvent; and Trp106 and Trp264, situated at the AC and AD interfaces, respectively Res. The AC interface, formed between two monomers along the tunnel axis, exhibits a large buried surface area ( $\sim$ 5200 Ų) and is stabilized by hydrogen bonds between the ends of the  $\beta$ -strands composing the  $\beta$ -barrel. On the other hand, the AD interface has a smaller buried area ( $\sim$ 800 Ų) and demarcates the region where the substrate accesses the active site Res. As shown in (Fig. 8), the relative decrease in intrinsic fluorescence emission of the Q269L mutant in comparison to WT-AFUOX suggests the repositioning of tryptophan residues in a more polar environment. These changes indicate the influence of the mutation on the protein structure, leading to local structural alterations.

The ANS fluorescence (as a charged hydrophobic fluorescent molecule) is used to identify hydrophobic pockets and compact and half-folded intermediates of the protein population. ANS (1-anilino-8-naphthalene sulfonate) binds to hydrophobic pockets on the protein surface, providing information about the exposed hydrophobic regions. As depicted in (Fig. 9), the comparison of external fluorescence spectra with the ANS control exhibited increased external fluorescence emission from the Q269L mutant protein compared to WT-AFUOX at different ANS concentrations. This indicates partial unfolding of the protein structure and increased exposure of hydrophobic pockets at the protein level. In other words, higher protein surface hydrophobicity, enhanced ANS binding, and consequently increased fluorescence were observed 69.

Fluorescence quenching in the presence of acrylamide was utilized to investigate the microenvironment surrounding tryptophan residues in the protein. Acrylamide and potassium iodide are commonly employed quenchers to reduce the fluorescence of tryptophan residues. Potassium iodide, due to its large size and charge, is restricted to quenching tryptophan residues either on the protein surface or near the surface. Conversely, acrylamide, being a small and neutral molecule, efficiently quenches tryptophan residues exposed to the solvent. Acrylamide can also penetrate the protein and quench the fluorescence of less exposed residues, albeit less effectively<sup>89</sup>. Quenching occurs when the quencher physically interacts with the indole ring of tryptophan, and the extent of quenching depends on the accessibility of the tryptophan residue to the solvent containing the quencher. This accessibility can be influenced by the distance of the tryptophan residue from the surface, its proximity to the surface, or its location within internal crevices of the protein.

The fluorescence quenching results using acrylamide and the corresponding Stern–Volmer plots at concentrations ranging from 0 to 900 mM are illustrated in (Fig. 10). The results demonstrate that the ratio ( $F_0/F$ ) increases with an increase in acrylamide concentration, indicating quenching effects for both the WT protein and the mutants. Figure 10 shows that the quenching effect of the Q269L mutant protein is more pronounced compared

	Assignment	Amide I position (cm <sup>-1</sup> )	Secondary structure %	
WT-AFUOX	β-Sheet	1630	52%	
	α-Helix	1653	21%	
	β-Turn	1671	17%	
	Random coil	1646	7%	
Q269L	β-Sheet	1633	44%	
	α-Helix	1653-1661	35%	
	β-Turn	1677	15%	
	Random coil	1640	6%	

**Table 4.** Assignment of amide I band components and percentages of secondary structure contents in WT-AFUOX and Q269L mutant.

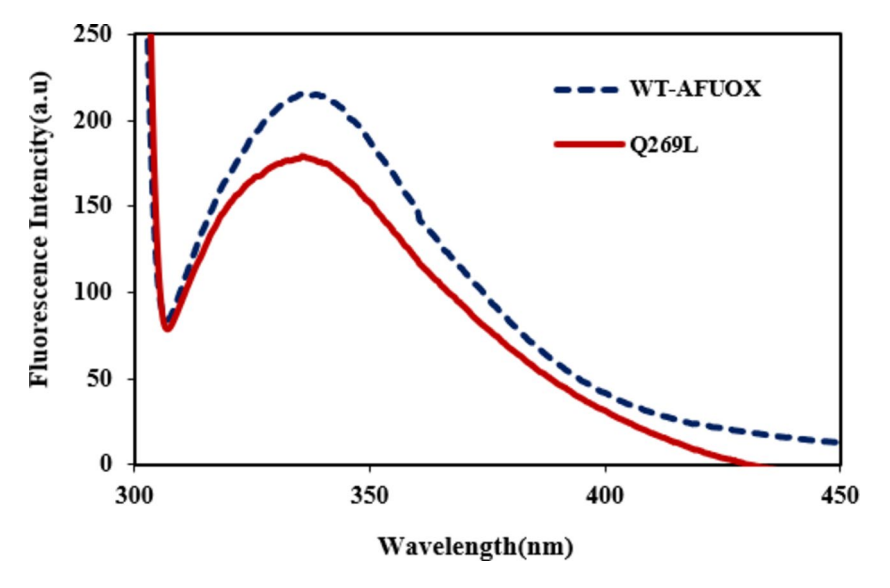


Fig. 8. Intrinsic fluorescence emission spectra (300–450 nm) of 20  $\mu$ g/ml WT-AFUOX and Q269L mutant in borate buffer (20 mM, pH 8.5 and 25 °C).

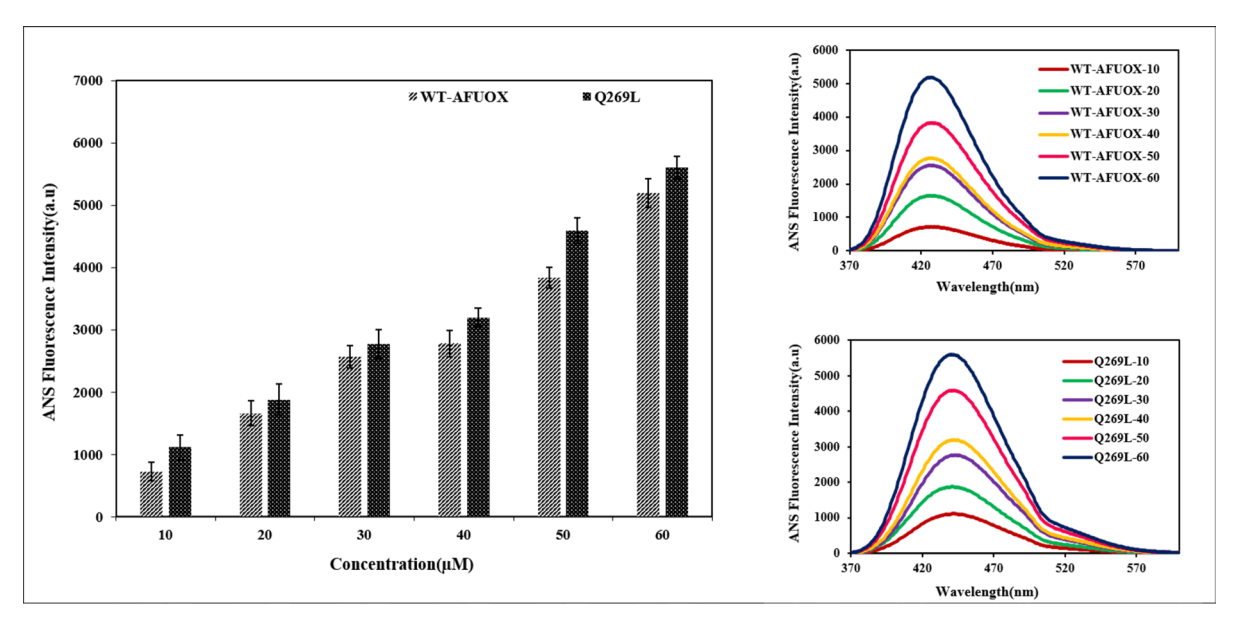
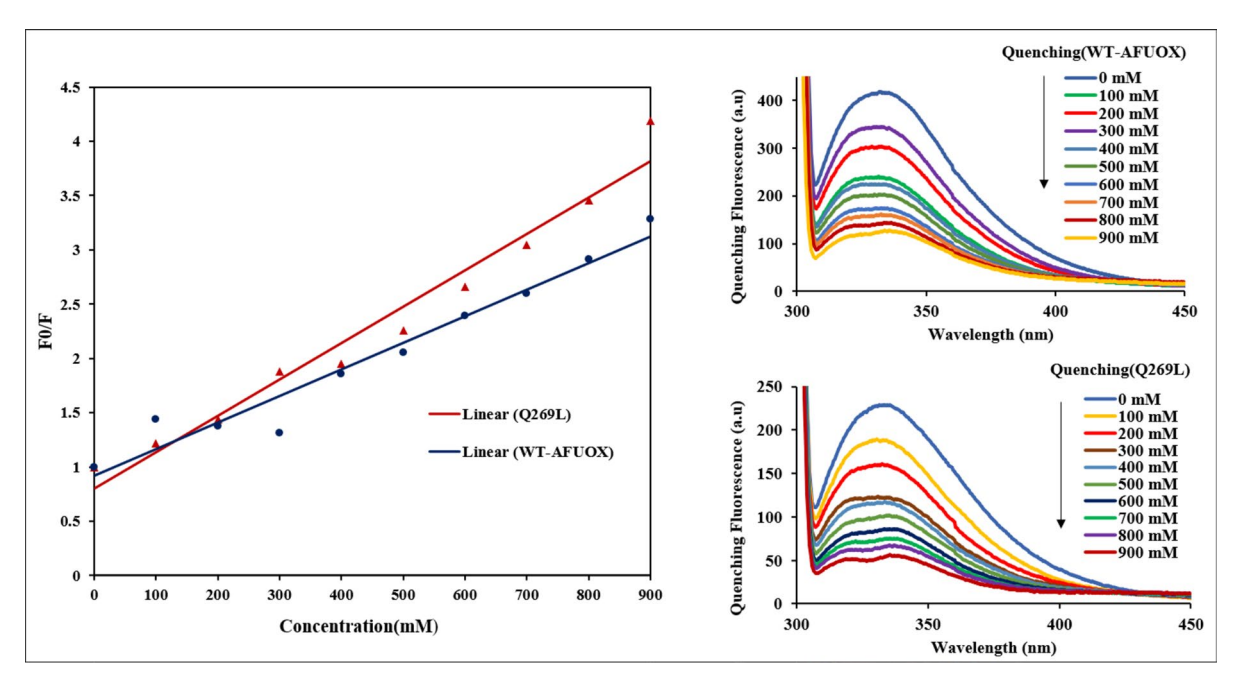


Fig. 9. The ANS fluorescence emission maximum of WT-AFUOX and Q269L mutant in borate buffer (20 mM, pH 8.5 and 25 °C). The concentration of UOX was 0.02 mg/ml. The inset shows ANS fluorescence emission spectra of WT-AFUOX and Q269L and the concentration of the ANS was 0–60  $\mu$ M (Error bars show the standard deviation of three independent measurements).

to the WT as the acrylamide concentration rises. Analysis of the Stern–Volmer quenching constant further confirms that the mutant protein exhibits higher quenching, indicating greater accessibility of the acrylamide quencher to tryptophan residues.

### Conclusion

Uricase, an enzyme with potential therapeutic applications, holds promise but faces challenges due to its low stability. This study aimed to investigate the structural impact of a mutation in UOX by substituting Gln 269 with Leu. Computational methods were employed to validate the effects of the mutation on protein dynamics and structure prediction. The dynamic analysis revealed significant structural differences between the WT-AFUOX and Q269L mutant in terms of RMSD, RMSF, SASA, Rg, and hydrogen bonding. Far-UV CD, extrinsic, and intrinsic fluorescence experiments demonstrated alterations in secondary structure components, increased levels of hydrophobic pockets, and a more polar environment for tryptophan residues in the Q269L mutant compared to WT-AFUOX. Thermal stability studies indicated greater stability of the mutant enzyme compared



**Fig. 10.** Stern–Volmer plot for quenching of WT-AFUOX and Q269L mutant by Acrylamide. The concentration of Acrylamide was from 0 to 900 mM and protein concentration was 0.02 mg/ml in 20 mM borate buffer pH 8.5 and 25 °C. The excitation and emission wavelengths were 295 and 340 nm, respectively. The arrow direction indicates an increase in Acrylamide concentration and a decrease in fluorescence emission.

to WT-AFUOX. The mutant enzyme exhibited maximum activity at higher temperatures and pH levels. Thermodynamic parameter analysis revealed a longer thermal half-life for the mutant enzyme. Overall, the mutation in UOX resulted in local conformational changes and improved stability compared to WT-AFUOX. These findings have implications for enhancing the accessibility and affordability of uricase, an important enzyme involved in the prevention and treatment of diseases like gout, which is currently a costly drug.

# Data availability

The datasets generated and/or analysed during the current study are available in the [Aspergillus flavus Uricase] repository, [https://www.uniprot.org/uniprotkb/Q00511/entry#sequences OR ACCESSION NUMBER; X61766.1 TO DATASETS]".

Received: 2 October 2024; Accepted: 6 February 2025 Published online: 10 March 2025

#### References

- 1. Li, J. et al. High-level expression, purification, and characterization of non-tagged Aspergillus flavus urate oxidase in Escherichia coli. *Protein Expr. Purif.* **49**, 55–59 (2006).
- 2. Cendron, L. et al. The structure of 2-oxo-4-hydroxy-4-carboxy-5-ureidoimidazoline decarboxylase provides insights into the mechanism of uric acid degradation. *J. Biol. Chem.* **282**, 18182–18189 (2007).
- 3. Collings, I. et al. Polymorphism of microcrystalline urate oxidase from Aspergillus flavus. *Acta Crystallogr. Sect. D Biol. Crystallogr.* **66**, 539–548 (2010).
- Li, W. et al. Directed evolution to improve the catalytic efficiency of urate oxidase from Bacillus subtilis. PLoS One 12, e0177877 (2017).
- Navolanic, P. et al. Elitek<sup>™</sup>-rasburicase: an effective means to prevent and treat hyperuricemia associated with tumor lysis syndrome, a Meeting Report, Dallas, Texas, January 2002. Leukemia 17, 499-514 (2003).
- Shaaban, M. I., Abdelmegeed, E. & Ali, Y. M. Cloning, expression, and purification of recombinant uricase enzyme from Pseudomonas aeruginosa Ps43 using Escherichia coli. J. Microbiol. Biotechnol. 25, 887–892 (2015).
- Xie, G. et al. Development of therapeutic chimeric uricase by exon replacement/restoration and site-directed mutagenesis. Int. J. Mol. Sci. 17, 764 (2016).
- 8. Montgomery, S. H., Capellini, I., Venditti, C., Barton, R. A. & Mundy, N. I. Adaptive evolution of four microcephaly genes and the evolution of brain size in anthropoid primates. *Mol. Biol. Evol.* 28, 625–638 (2011).
- 9. King, C. et al. Uric acid as a cause of the metabolic syndrome. Uric Acid Chronic Kidney Dis. 192, 88-102 (2018).
- 10. Singh, G., Lingala, B. & Mithal, A. Gout and hyperuricaemia in the USA: prevalence and trends. *Rheumatology* **58**, 2177–2180 (2019).
- Liu, X. et al. High-yield expression, purification, characterization, and structure determination of tag-free Candida utilis uricase. Appl. Microbiol. Biotechnol. 92, 529–537 (2011).
- 12. Aly, M., Tork, S., Al-Garni, S. & Allam, R. Production and characterization of uricase from Streptomyces exfoliatus UR10 isolated from farm wastes. *Turk. J. Biol.* 37, 520–529 (2013).
- 13. Legoux, R. et al. Cloning and expression in Escherichia coli of the gene encoding Aspergillus flavus urate oxidase. *J. Biol. Chem.* **267**, 8565–8570 (1992).

- Yainoy, S. et al. Production and characterization of recombinant wild type uricase from indonesian coelacanth (L. menadoensis) and improvement of its thermostability by in silico rational design and disulphide bridges engineering. *Int. J. Mol.Sci.* 20, 1269 (2019).
- 15 Ålakel, N., Middeke, J. M., Schetelig, J. & Bornhäuser, M. Prevention and treatment of tumor lysis syndrome, and the efficacy and role of rasburicase. *OncoTargets Ther.* **10**, 597–605 (2017).
- 16. FitzGerald, O., Fitzpatrick, D. & McGeeney, K. Urate-oxidase treatment for hyperuricaemia. Lancet 305, 525 (1975).
- 17. Gabison, L. et al. Near-atomic resolution structures of urate oxidase complexed with its substrate and analogues: the protonation state of the ligand. Acta Crystallogr. Sect. D Biol. Crystallogr. 66, 714–724 (2010).
- 18. Retailleau, P. et al. Urate oxidase from Aspergillus flavus: new crystal-packing contacts in relation to the content of the active site. *Acta Crystallogr. Sect. D Biol. Crystallogr.* **61**, 218–229 (2005).
- 19. Fazel, R. et al. Cloning and expression of Aspergillus flavus urate oxidase in Pichia pastoris. Springerplus 3, 1-7 (2014).
- Retailleau, P. et al. Complexed and ligand-free high-resolution structures of urate oxidase (Uox) from Aspergillus flavus: a reassignment of the active-site binding mode. Acta Crystallogr. Sect. D Biol. Crystallogr. 60, 453–462 (2004).
- 21. Goldman, S. C. et al. A randomized comparison between rasburicase and allopurinol in children with lymphoma or leukemia at high risk for tumor lysis: Presented in part at the American Society of Hematology Conference in Miami Beach, FL, December 1998. *Blood J. Am. Soc. Hematol.* **97**, 2998–3003 (2001).
- 22. Pui, C., Jeha, S., Irwin, D. & Camitta, B. Recombinant urate oxidase (rasburicase) in the prevention and treatment of malignancy-associated hyperuricemia in pediatric and adult patients: results of a compassionate-use trial. *Leukemia* 15, 1505–1509 (2001).
- Balabanova, L., Golotin, V., Podvolotskaya, A. & Rasskazov, V. Genetically modified proteins: functional improvement and chimeragenesis. Bioengineered 6, 262–274 (2015).
- 24. Akbarian, M. & Chen, S.-H. Instability challenges and stabilization strategies of pharmaceutical proteins. *Pharmaceutics* 14, 2533 (2022).
- 25. Cammalleri, L. & Malaguarnera, M. Rasburicase represents a new tool for hyperuricemia in tumor lysis syndrome and in gout. Int. J. Med. Sci. 4, 83 (2007).
- Baziyar, P., Seyedalipour, B. & Hosseinkhani, S. Zinc binding loop mutations of hSOD1 promote amyloid fibrils under physiological conditions: Implications for initiation of amyotrophic lateral sclerosis. *Biochimie* 199, 170–181 (2022).
- 27. Kadokura, H., Katzen, F. & Beckwith, J. Protein disulfide bond formation in prokaryotes. Annu. Rev. Biochem. 72, 111-135 (2003).
- 28 Mavadat, E., Seyedalipour, B. & Hosseinkhani, S. A double point mutation of SOD1 targeting net charge promotes aggregation under destabilizing conditions: Correlation of charge distribution and ALS-provoking mutation. *Biochim. Biophys. Acta (BBA)* Gen. Subj. 1867, 130325 (2023).
- Pazhang, M. Study of the stability of uricase from Aspergillus flavus and its stabilization by Glucose. Modares J. Biotechnol. 8, 50–60 (2017).
- 30. Feller, G. Protein stability and enzyme activity at extreme biological temperatures. J. Phys. Condens. Matter 22, 323101 (2010).
- 31. Khalifeh, K., Ranjbar, B., Alipour, B. S. & Hosseinkhani, S. The effect of surface charge balance on thermodynamic stability and kinetics of refolding of firefly luciferase. *BMB Rep.* 44, 102–106 (2011).
- 32. Marsh, J. A. Buried and accessible surface area control intrinsic protein flexibility. J. Mol. Biol. 425, 3250-3263 (2013).
- 33. Sanchez-Ruiz, J. M. Protein kinetic stability. Biophys. Chem. 148, 1-15 (2010).
- 34. Wong, E. T., Na, D. & Gsponer, J. On the importance of polar interactions for complexes containing intrinsically disordered proteins. *PLoS Comput. Biol.* **9**, e1003192 (2013).
- 35. Din, S. M. U., Shan, K., Rehman, T. U., Ivanov, S. & Vargas-Madueno, F. M. Unexpected rasburicase-induced hemolysis in a patient with normal glucose-6-phosphate dehydrogenase activity. *J. Med. Cases* 15, 231 (2024).
- Beedkar, S. D., Khobragade, C., Bodade, R. G. & Vinchurkar, A. S. Comparative structural modeling and docking studies of uricase: possible implication in enzyme supplementation therapy for hyperuricemic disorders. Comput. Biol. Med. 42, 657–666 (2012).
- Karshikoff, A. & Ladenstein, R. Ion pairs and the thermotolerance of proteins from hyperthermophiles: a 'traffic rule'for hot roads.
   Trends Biochem. Sci. 26, 550-557 (2001).
- 38. Pappenberger, G., Schurig, H. & Jaenicke, R. Disruption of an ionic network leads to accelerated thermal denaturation of D-glyceraldehyde-3-phosphate dehydrogenase from the hyperthermophilic bacterium Thermotoga maritima. *J. Mol. Biol.* **274**, 676–683 (1997)
- 39. Xiao, L. & Honig, B. Electrostatic contributions to the stability of hyperthermophilic proteins. J. Mol. Biol. 289, 1435-1444 (1999).
- 40. Jelesarov, I. & Karshikoff, A. Defining the role of salt bridges in protein stability. In *Protein Structure, Stability, and Interactions* (ed. Shriver, J. W.) 227–260 (Humana Press, 2009).
- 41. Chen, C.-W., Lin, J. & Chu, Y.-W. In BMC bioinformatics, 1-14 (Springer).
- 42. Taherimehr, Z., Zaboli, M. & Torkzadeh-Mahani, M. New insight into the molecular mechanism of the trehalose effect on urate oxidase stability. *J. Biomol. Struct. Dyn.* 40, 1461–1471 (2022).
- 43. Abraham, M. J. et al. GROMACS: High performance molecular simulations through multi-level parallelism from laptops to supercomputers. *SoftwareX* 1, 19–25 (2015).
- 44. Case, D. A. et al. The Amber biomolecular simulation programs. J. Comput. Chem. 26, 1668-1688 (2005).
- 45 Bussi, G., Donadio, D. & Parrinello, M. Canonical sampling through velocity rescaling. *J. Chem. Phys.* https://doi.org/10.1063/1. 2408420 (2007).
- 46. Muthukumar, V. C. The dynamics of Escherichia coli FtsZ dimer. J. Biomol. Struct. Dyn., 1-14 (2023).
- 47 Imani, M. & Shahmohamadnejad, S. Recombinant production of Aspergillus Flavus uricase and investigation of its thermal stability in the presence of raffinose and lactose. 3 Biotech 7, 1–9 (2017).
- 48. Imani, M., Pazhang, M. & Mirzaeinia, S. Cloning and expression of therapeutic enzyme, Aspergillus Flavus Uricase in E. coli. J. Adv. Med. Biomed. Res. 24, 109–121 (2016).
- 49. Koyama, Y., Ichikawa, T. & Nakano, E. Cloning, sequence analysis, and expression in Escherichia coli of the gene encoding the Candida utilis urate oxidase (uricase). *J. Biochem.* **120**, 969–973 (1996).
- Deshpande, M. & Sathe, S. K. Interactions with 8-Anilinonaphthalene-1-sulfonic Acid (ANS) and Surface Hydrophobicity of Black Gram (Vigna mungo) Phaseolin. J. Food Sci. 83, 1847–1855 (2018).
- 51. Cioni, P. & Strambini, G. B. Acrylamide quenching of protein phosphorescence as a monitor of structural fluctuations in the globular fold. *J. Am. Chem. Soc.* **120**, 11749–11757 (1998).
- 52 Lakowicz, J. R. Principles of Fluorescence Spectroscopy (Springer, 2006).
- 53. Mauerer, A. & Lee, G. Changes in the amide I FT-IR bands of poly-l-lysine on spray-drying from α-helix, β-sheet or random coil conformations. *Eur. J. Pharm. Biopharm.* **62**, 131–142 (2006).
- 54. Arrhenius, S. About the reaction rate during the inversion of cane sugar through acids. Z. Phys. Chem. 4 (1889).
- 55. Marin, E., Sanchez, L., Perez, M., Puyol, P. & Calvo, M. Effect of heat treatment on bovine lactoperoxidase activity in skim milk: kinetic and thermodynamic analysis. *J. Food Sci.* **68**, 89–93 (2003).
- Galani, D. & Apenten, R. K. O. The comparative heat stability of bovine β-lactoglobulin in buffer and complex media. J. Sci. Food Agric. 74, 89–98 (1997).
- 57. Rashid, F., Sharma, S. & Bano, B. Comparison of guanidine hydrochloride (GdnHCl) and urea denaturation on inactivation and unfolding of human placental cystatin (HPC). *Protein J.* 24, 283–292 (2005).

- 58. Hiromasa, Y., Meno, K. & Aso, Y. Denaturation of the Bacillus stearothermophilus dihydrolipoamide dehydrogenase in the presence of guanidine-HCl at low temperature (2003).
- 59 Scholtz, J. M., Grimsley, G. R. & Pace, C. N. Methods in Enzymology Vol. 466, 549-565 (Elsevier, 2009).
- 60. Sonkar, K. S., Pachauri, M., Kumar, A., Choudhary, H. & Jagannadham, M. V. Conformational stability of peroxidase from the latex of Artocarpus lakoocha: influence of pH, chaotropes, and temperature. *Front. Plant Sci.* 15, 1341454 (2024).
- 61. Compiani, M. & Capriotti, E. Computational and theoretical methods for protein folding. Biochemistry 52, 8601-8624 (2013).
- 62. Martelli, P. L. et al. Large scale analysis of protein stability in OMIM disease related human protein variants. *BMC Genom.* 17, 239–247 (2016).
- 63. Stefl, S., Nishi, H., Petukh, M., Panchenko, A. R. & Alexov, E. Molecular mechanisms of disease-causing missense mutations. *J. Mol. Biol.* 425, 3919–3936 (2013).
- 64. Tian, R., Basu, M. K. & Capriotti, E. Computational methods and resources for the interpretation of genomic variants in cancer. *BMC Genom.* **16**. S7 (2015).
- 65. Van Gunsteren, W. F. et al. Biomolecular modeling: goals, problems, perspectives. Angew. Chem. Int. Ed. 45, 4064–4092 (2006).
- 66. Monroe, J. I. & Shirts, M. R. Converging free energies of binding in cucurbit [7] uril and octa-acid host-guest systems from SAMPL4 using expanded ensemble simulations. *J. Comput. Aided Mol. Des.* 28, 401-415 (2014).
- 67. Hendam, A., Al-Sadek, A. F. & Hefny, H. A. Molecular dynamic simulation of neurexin1α mutations associated with mental disorder. *J. Mol. Neurosci.* **72**, 2252–2272 (2022).
- Ghanbari-Ardestani, S. et al. The effect of different percentages of triethanolammonium butyrate ionic liquid on the structure and activity of urate oxidase: Molecular docking, molecular dynamics simulation, and experimental study. J. Mol. Liquids 292, 111318 (2019).
- 69. Shahmoradipour, P., Zaboli, M. & Torkzadeh-Mahani, M. Exploring the impact of taurine on the biochemical properties of urate oxidase: response surface methodology and molecular dynamics simulation. *J. Biol. Eng.* **18**, 10 (2024).
- 70. Roccatano, D. A short introduction to the molecular dynamics simulation of nanomaterials. Micro Nanomanuf. II, 123-155 (2018).
- 71. Baammi, S., Daoud, R. & El Allali, A. In silico protein engineering shows that novel mutations affecting NAD+ binding sites may improve phosphite dehydrogenase stability and activity. Sci. Rep. 13, 1878 (2023).
- Moradi, S., Hosseini, E., Abdoli, M., Khani, S. & Shahlaei, M. Comparative molecular dynamic simulation study on the use of chitosan for temperature stabilization of interferon αII. Carbohydr. Polym. 203, 52–59 (2019).
- 73. Carlsson, A.-C.C. et al. Increasing enzyme stability and activity through hydrogen bond-enhanced halogen bonds. *Biochemistry* 57, 4135–4147 (2018).
- 74. Jiang, Z., You, L., Dou, W., Sun, T. & Xu, P. Effects of an electric field on the conformational transition of the protein: A molecular dynamics simulation study. *Polymers* 11, 282 (2019).
- Pikkemaat, M. G., Linssen, A. B., Berendsen, H. J. & Janssen, D. B. Molecular dynamics simulations as a tool for improving protein stability. *Protein Eng.* 15, 185–192 (2002).
- 76. Zaboli, M., Raissi, H., Zaboli, M., Farzad, F. & Torkzadeh-Mahani, M. Stabilization of D-lactate dehydrogenase diagnostic enzyme via immobilization on pristine and carboxyl-functionalized carbon nanotubes, a combined experimental and molecular dynamics simulation study. *Arch. Biochem. Biophys.* 661, 178–186 (2019).
- 77. Mirzaeinia, S., Pazhang, M., Imani, M., Chaparzadeh, N. & Amani-Ghadim, A. R. Improving the stability of uricase from Aspergillus flavus by osmolytes: Use of response surface methodology for optimization of the enzyme stability. *Process Biochem.* **94**, 86–98 (2020)
- 78 Kielkopf, C. L., Bauer, W. & Urbatsch, I. L. Bradford assay for determining protein concentration. *Cold Spring Harbor Protocols* **2020**, pdb. prot102269 (2020).
- 79. Marjani, L. R., Imani, M. & Jaliani, H. Z. Enhancement of pharmaceutical urate oxidase thermostability by rational design of de novo disulfide bridge. *Iran. J. Biotechnol.* 18, e2662 (2020).
- 80. Bhuyan, A. K. Protein stabilization by urea and guanidine hydrochloride. Biochemistry 41, 13386-13394 (2002).
- 81. Povarova, O. I., Kuznetsova, I. M. & Turoverov, K. K. Differences in the pathways of proteins unfolding induced by urea and guanidine hydrochloride: molten globule state and aggregates. *PLoS One* 5, e15035 (2010).
- 82 Vecchio, P. D. et al. Denaturing action of urea and guanidine hydrochloride towards two thermophilic esterases. *Biochem. J.* **367**, 857–863 (2002).
- 83. Greenfield, N. J. Using circular dichroism spectra to estimate protein secondary structure. Nat. Protocols 1, 2876-2890 (2006).
- 84. Zou, Y. & Ma, G. A new criterion to evaluate water vapor interference in protein secondary structural analysis by FTIR spectroscopy. *Int. J. Mol. Sci.* 15, 10018–10033 (2014).
- 85 Byler, D. M. & Susi, H. Examination of the secondary structure of proteins by deconvolved FTIR spectra. *Biopolym. Orig. Res. Biomol.* 25, 469–487 (1986).
- 86 Chirgadze, Y. N. & Nevskaya, N. Infrared spectra and resonance interaction of amide-I vibration of the antiparallel-chain pleated sheet. *Biopolym. Orig. Res. Biomol.* **15**, 607–625 (1976).
- 87. Jackson, M. & Mantsch, H. H. The use and misuse of FTIR spectroscopy in the determination of protein structure. *Crit. Rev. Biochem. Mol. Biol.* 30, 95–120 (1995).
- 88. Girard, E. et al. Structure-function perturbation and dissociation of tetrameric urate oxidase by high hydrostatic pressure. *Biophys. J.* **98**, 2365–2373 (2010).
- 89. Phillips, S., Wilson, L. & Borkman, R. Acrylamide and iodide fluorescence quenching as a structural probe of tryptophan microenvironment in bovine lens crystallins. *Curr. Eye Res.* 5, 611–620 (1986).

# **Acknowledgements**

The authors would like to express their gratitude to the Research Council of Mazandaran University for their support in this work. We also would like to express our gratitude to Mr. Salarieh for his valuable assistance with FTIR.

# **Author contributions**

M. A: Methodology, perform experiments, data curation, Validation, writing—original draft preparation; B. S: Conceptualization, Supervision, Visualization, Validation, data curation, formal analysis, writing –review & editing; M. P: Conceptualization, Validation, data curation, formal analysis, writing –review & editing; M. I: Data curation, formal analysis, writing –review & editing. All authors reviewed the manuscript.

#### **Declarations**

# Competing interests

The authors declare no competing interests.

#### Additional information

**Supplementary Information** The online version contains supplementary material available at https://doi.org/10.1038/s41598-025-89605-w.

Correspondence and requests for materials should be addressed to B.S.

Reprints and permissions information is available at www.nature.com/reprints.

**Publisher's note** Springer Nature remains neutral with regard to jurisdictional claims in published maps and institutional affiliations.

**Open Access** This article is licensed under a Creative Commons Attribution-NonCommercial-NoDerivatives 4.0 International License, which permits any non-commercial use, sharing, distribution and reproduction in any medium or format, as long as you give appropriate credit to the original author(s) and the source, provide a link to the Creative Commons licence, and indicate if you modified the licensed material. You do not have permission under this licence to share adapted material derived from this article or parts of it. The images or other third party material in this article are included in the article's Creative Commons licence, unless indicated otherwise in a credit line to the material. If material is not included in the article's Creative Commons licence and your intended use is not permitted by statutory regulation or exceeds the permitted use, you will need to obtain permission directly from the copyright holder. To view a copy of this licence, visit http://creativecommons.org/licenses/by-nc-nd/4.0/.

© The Author(s) 2025